MODELS AND CONSTRAINTS FOR NEW PHYSICS AT THE ENERGY, INTENSITY, AND COSMIC FRONTIERS

by

GREGORY BARELLO

A DISSERTATION

Presented to the Department of Physics
and the Graduate School of the University of Oregon
in partial fulfillment of the requirements
for the degree of
Doctor of Philosophy

June 2016

DISSERTATION APPROVAL PAGE

Student: Gregory Barello

Title: Models and Constraints for New Physics at the Energy, Intensity, and Cosmic Frontiers

This dissertation has been accepted and approved in partial fulfillment of the requirements for the Doctor of Philosophy degree in the Department of Physics by:

Graham Kribs	Chair
Spencer Chang	Advisor
Stephanie Majewski	Core Member
Boris Botvinnik	Institutional Representative

and

Scott L. Pratt	Dean of the Graduate School

Original approval signatures are on file with the University of Oregon Graduate School.

Degree awarded June 2016

DISSERTATION ABSTRACT

Gregory Barello

Doctor of Philosophy

Department of Physics

June 2016

Title: Models and Constraints for New Physics at the Energy, Intensity, and Cosmic Frontiers

The modern era of particle physics is driven by experimental anomalies. Experimental efforts have become increasingly diverse and are producing enormous volumes of data. In such a highly data-driven scientific environment theoretical models are necessary to understand this data and to help inform the development of new experimental approaches. In this dissertation I present two significant contributions to this effort relevant to the energy, intensity, and cosmic frontiers of modern particle physics research.

Part 1 of this dissertation discusses methods to understand modern dark matter direct detection results. In particular I present an analysis under the hypothesis of inelastic dark matter, which supposes that dark matter must scatter inelastically, i.e. that it must gain or loose mass during a collision with atomic nuclei. This hypothesis is attractive because it can alleviate otherwise contradictory results from a number of dark matter detection facilities. The main conclusion of this work is a presentation of the analytical tools, along with a mathematica package that can be used to run the analysis, and the discovery that there are regions of inelastic dark matter parameter

space which are consistent with all current experimental results, and constraints.

Part 2 of this dissertation discusses a phenomenon of modern interest called kinetic mixing which allows particles from the standard model to spontaneously transform into particles which experience a new, as of yet undiscovered, force. This phenomenon is relatively common and well motivated theoretically and has motivated significant experimental effort. In this work, I present an analysis of a general case of kinetic mixing, called nonabelian kinetic mixing. This work shows that, In general, kinetic mixing predicts the existence of a new particle and that, under certain conditions, this particle could be detected at modern particle colliders. Furthermore, the mass of this particle is related to the strength of kinetic mixing. This relationship suggests novel ways to constrain kinetic mixing parameter space, and if observed would provide a very striking indication that such a model is realized in nature.

This dissertation includes previously published and unpublished co-authored material.

CURRICULUM VITAE

NAME OF AUTHOR: Gregory Barello

GRADUATE AND UNDERGRADUATE SCHOOLS ATTENDED:

University of Oregon, Eugene, Oregon
Reed College, Portland, Oregon

DEGREES AWARDED:

Doctor of Philosophy, Physics, 2016, University of Oregon
Bachelor of Science, Mathematics and Physics, 2012, Reed College

PROFESSIONAL EXPERIENCE:

Graduate Research Assistant, University of Oregon, 2013 to 2016

Graduate Teaching Fellow, University of Oregon, 2012-2016

GRANTS, AWARDS AND HONORS:

PITT PACC Travel Grant 2016

National Institutes Summer Fellow 2015

Science Literacy Program Fellow 2014, 2015, 2016

PUBLICATIONS:

G. Barello, Spencer Chang, and Christopher A. Newby. Correlated Signals at the Energy and Intensity Frontiers from Nonabelian Kinetic Mixing. 2015.

G. Barello, Spencer Chang, and Christopher A. Newby. A Model Independent Approach to Inelastic Dark Matter Scattering. Phys. Rev., D90(9):094027, 2014.

ACKNOWLEDGEMENTS

There are many people whose influence on my life merits acknowledgement. Really, if I had the space and memory for it I would ideally like to mention everyone. As it stands, I'll just go for the most recent and relevant.

First and foremost, I would like to mention my loving family; Larry Barello, Leigha Krueger, and Kadee Barello. I have done a lot of stupid, risky, things in my life, many but not all of which turned out OK. Their love and support has given me the stability and confidence to take those risks, many of which made my life what it is today. I love you mother, father, sister.

Next I'd like to give a shout out to my academic mentors. Firstly there is of course Spencer Chang, who guided me through my graduate school experience. He agreed my first year to supervise a reading course in quantum field theory. I believe that experience and the connection we developed through it provided the framework for me to become active in research. He has also just all around been a great advisor, enthusiastically providing guidance when needed, and encouraging of my exploration of physics, and other fields. Another person who deserves special mention is David Latimer, my friend and undergraduate thesis advisor. He in fact guided my first foray into quantum field theory, and supervised my first independent research project. He is a fantastic example of what it means to be an excellent academic and excellent human.

The research I have been involved with would not be a fraction its quality if it weren't for the involvement of my collaborators, most notably Chris A. Newby,

Spencer S. Chang, and Bryan M. Ostdiek. They have respectfully pointed out every mistake I've made and just generally made living on the fourth floor more bearable, especially since Chris put a couch in his office.

Despite my love of physics, and general desire for an understanding of the universe, I am only able to dedicate the fraction of my life that I do to it because the rest of my life is also so full of love and friendship. Lets start with the person who is closest to me physically; S.P. He is a lovely man who I've spend a large fraction of the last three years within three feet of. His undying cynicism really makes this dark, windowless, office feel cheery and gay by comparison. But seriously S.P. your companionship means a lot to me. Next I'll go for he who has known me the longest: Wesley Erickson. He was there my first day of undergrad and, although we haven't been the best of friends *ever* since, things have really come around since then. We lived together eight years ago in Portland, and again two years ago in Eugene, we stole money from casinos and shot arrows at watermelons. We are still, and will continue to be, very close friends. I'm looking forward to spending some of my summer in Europe with you, bro. My final graduate student companion who deserves a special mention is George de Coster. He is a compassionate, intelligent, and romantic man and I expect my life to continue to be enriched my his friendship. Also; we can't stop being friends till I beat you at squash, so i'm in it for the long-haul. Spending time with you this summer would be great, too, if you weren't so distracted by *that girl*. A special shout out to all my dancing friends, you know who you are. Those friends who I rarely see, but are still dear to me: Kate Kourbatova, Jake Burton, Tiriel Gould, Moriah Tobin. And finally there some people who I don't see much at all anymore, but whom I still care for very deeply; Aya Maguire, Madeline Brandt.

TABLE OF CONTENTS

LIST OF FIGURES

Figure Page

LIST OF TABLES

Table Page

CHAPTER I

INTRODUCTION

The State of Particle Physics

The Standard Model of Particle Physics has guided high energy particle physics research for the last four decades. Since its development in the 1970s every test of the Standard Model has confirmed its predictions, culminating in the 2012 discovery of the Higgs boson at the Large Hadron Collider [1]. The Standard Model is our most fundamental theory of the constituents of matter, and yet, there are phenomena that it cannot explain. For decades the goal of validating the Standard Model has guided theoretical and experimental particle physics. Now most of the predictions of the Standard Model have been verified, and there are only unexplained phenomena in need of an understanding. This is the state that particle physics finds itself in today.

Some of the phenomena in need of an explanation are: neutrino masses, the hierarchy problem, and dark matter. These are the driving forces behind the theoretical and experimental research that occurs today. Within the standard model, neutrinos are predicted to be massless, however recent measurements of neutrino oscillations imply that the neutrinos do have a (very small) mass [2]. The hierarchy problem refers to a theoretical difficulty with the standard model, whereby the parameters of the model must be very finely tuned in order to produce the light Higgs boson that has been discovered. Dark matter will be one main focus of this thesis. Dark matter refers to the observation that 80% of the matter in our universe seems to be made up of something which is not the standard model material that

we know of. On the other hand there are experimental facilities producing fantastic volumes of data. In such a data-driven scientific environment it is important for theorists to develop models which can be used to guide scientific efforts. This is the point of view I have taken during my own work. My work has focused on developing interesting and useful phenomenological predictions, with a special focus on dark matter and related phenomena.

On the experimental side it is important to cast a wide net which has motivated a multi-pronged approach highlighting three main categories: the energy, intensity, and cosmic frontiers [3].

The energy frontier: Those experiments which aim to create extremely energetic collisions of particles are collectively known as energy frontier experiments. The primary examples of such an experiment are those associated with particle colliders, such as ATLAS and CMS located at the Large Hadron Collider, which are relevant to the material presented in part 2 of this document. The most significant energy frontier experiment in operation is the Large Hadron Collider (LHC) which collides beams of protons at a center-of-mass energy of 13TeV; $13,000$ times the proton mass.

The intensity frontier: Those experiments which aim to measure extremely rare, or weak, phenomena by taking advantage of very high intensity sources of particles are part of the intensity frontier. Examples of these experiments include fixed-target collider experiments, such as those discussed in part 2 of this document, and reactor-based neutrino experiments, which work with very high luminosity beams

of neutrinos, such as BooNE, located at Fermilab.

The cosmic frontier: Those experiments which take advantage of the many physical processes which happen in the cosmos to obtain their data comprise the so-called cosmic frontier. Part 1 of this document will discuss one particular type: the dark matter direct detection facilities, such as XENON, LUX, DAMA/LIBRA, and others. These experiments rely on the presence of dark matter in our local environment to be able to detect collisions between the dark matter and standard nuclear matter, and have been the focus of my work. Other examples of cosmic frontier experiments, which are featured less heavily in my research, are neutrino detection facilities, such as IceCube Neutrino Observatory, and various telescopes in operation, such as AMS, FERMI, and others.

Overview

This dissertation discusses two main threads within beyond the Standard Model (BSM) phenomenology.

Dark Matter Direct Detection

Dark matter is a well established reality (see [4] and references therein). The original hints of dark matter were from discrepancies in the orbital velocities of celestial bodies. Since then indications of dark matter have been measured via gravitational effects, and the most successful models of cosmology include dark matter, and provide remarkably good explanations of elemental abundances, and anisotropies in the cosmic microwave background. It is widely believed that dark

matter is particulate in nature. This conclusion is supported by the mass distribution of the famous bullet cluster [5], as well as the fantastic agreement between the cosmic microwave background anisotropy spectrum and predictions made by cosmological models incorporating particulate dark matter [6]. More recently there have been a number of anomalous measurements which may be the first hint of dark matter, both in ground based, direct detection experiments [7], and from studies of cosmic radiation [8]. So far, the unambiguous evidence we have for dark matter is mostly due to it's extremely weak, gravitational, interaction with the Standard Model.

Naturally, this breadth of evidence, and contemporary hints of a signal, have induced a flurry of theoretical and experimental developments. There are three main approaches taken when trying to study dark matter. The first is the so-called indirect detection, in which one hopes to observe the Standard Model remnants of dark matter interactions in the cosmos. Experimentally, this subfield is represented mostly by telescopes, such as FERMI/LAT [9], and AMS-2 [10]. The second significant effort is so-called direct production, in which the hope is to be able to produce dark matter at particle colliders, and see traces of it in the collision events. The third cornerstone of the modern experimental effort is direct detection, which will be the focus of the work presented here, and involves monitoring large volumes of Standard Model matter in hopes of witnessing a collision event with dark matter. The assumption underlying all of these approaches is that dark matter does interact with the Standard Model in some manner other than gravitationally. Indeed, if it did not there would be little hope of detecting dark matter for the foreseeable future. Guided by this assumption, direct detection experiments place a large volume of Standard Model material (examples include xenon, and crystalline scintillators made out of various

salts) in a low background environment, commonly at the bottom of a mine shaft, deep underground, and monitor it for unexpected collision events.

Many direct detection experiments have already been built and the results are mixed. Most experiments report no signal while others report a persistent signal, seemingly in conflict with others' null result. One complicating factor is that different experiments have chosen different materials to use as their detection medium. In the simplest case, scattering in these different materials should interact in comparable ways with dark matter, and this is the interpretation used to compute most exclusions. On the other hand, more complex models of dark matter often predict that the strength of a dark matter particle's interaction can vary widely depending on the details of the atomic nuclei being used. Models of dark matter have begun to take advantage of this complexity in order to explain how some experiments see a signal while others do not. As a matter of fact, using a diverse range of materials has the advantage of potentially being sensitive to a wider range of dark matter models.

One way to gain a handle on the effects of different materials is to decompose the response of the nucleus into so-called form factors of the nuclei. These form factors can in principle be computed for various nuclei, and each form factor couples only to a specific set of dark matter - Standard Model interactions. Then dark matter interactions can be categorized by which couple to each form factor. This allows us to study the coupling operators themselves, and then use our knowledge of each material to apply the results to specific experiments effectively decoupling the process of analyzing dark matter interactions from applying those analyses to specific materials. Furthermore, effective field theory allows us to parameterize all

possible interactions of dark matter in terms of these operators which couple to the form factors in a well defined way, allowing us to perform a fully model independent analysis of each operator, and then make the link to particular models after the fact. This approach has found success in the study of dark matter direct detection, as well as other applications [11, 12]. This parameterization can be used both to guide experimental efforts, and to guide model building efforts. The details of this approach will be discussed in chapter 2, and references therein.

The work presented in chapter 2 goes one step further by applying this technique to a promising explanation of modern direct detection results: inelastic dark matter. Inelastic dark matter refers to the possibility that dark matter undergoes inelastic scattering: a reaction in which the dark matter must change form to another, slightly heavier, dark matter particle while interacting with Standard Model particles. It was realized some time ago that inelastic scattering can ameliorate current contradictory results [13]. Applying the analysis presented here allows direct detection of inelastic dark matter to be understood in a model-independent way. Our results are presented in chapter 2.

Kinetic Mixing at the Energy and Intensity Frontiers

The second thread of this dissertation is the study of kinetic mixing. To understand the relevance of kinetic mixing it must be understood that in particle physics there are a number of common motifs. One of the most fundamental is that of the gauge force. All of the strong, weak, and electromagnetic forces are described as gauge forces. The success of gauge theory in our current models of physics suggests that it will continue to appear in the new physics that we discover. Importantly,

there are many concrete predictions we can make on the basis of gauge theory. One prime example is kinetic mixing, which was first discussed by B. Holdom in 1985 [14]. Kinetic mixing is a phenomenon in which a new gauge boson can spontaneously turn into a photon, or other Standard Model gauge boson, and will generically occur whenever a new abelian gauge force is present. This phenomenon straightforwardly generalizes to nonabelian gauge theories as well. In addition to its naturalness in BSM models, kinetic mixing can be part of a suitable description of dark matter interacting with the Standard Model, which can even generate the inelastic transitions discussed before [15].

The new gauge forces required to generate kinetic mixing are naturally present in many BSM physics theories, especially dark matter models where it may be that an entire "dark sector" exists with many particles and gauge forces. It has also long been hoped that kinetic mixing could ameliorate conflict between the Standard Model and the measured anomalous magnetic moment of the muon [16]. Indeed, there are values of the new boson's mass and kinetic mixing strength which can fully account for the muon anomalous magnetic moment. However, as it stands, the preferred regions are ruled out for the simplest kinetic mixing models. In addition to this, models with kinetic mixing are able to accommodate recent anomalies seen in cosmic rays [10, 17, 18].

These facts, as well as a healthy body of theoretical work which incorporates kinetic mixing, has encouraged the development of a large experimental effort specifically searching for kinetic mixing, which spans the intensity and energy frontiers. The approach this dissertation will focus on recognizes that the new gauge

boson, once created, will eventually decay into Standard Model particles, as long as it is sufficiently heavy to do so. This is the idea behind studies at the LHC, which look for "lepton-jets", which are created when a high energy dark photon decays to a collimated spray of electrons or muons that appears inside their detector. At the intensity frontier, beam-dump and fixed-target facilities use the fact that the dark photon will interact weakly with the Standard Model to take advantage of a shield, collide a particle beam with it, and see if anything comes out the other side (see, for example, [19]). If a dark photon does exist and couples sufficiently weakly to the Standard Model it will travel through the shield and decay to electrons, or muons, on the other side. The length and nature of decay depends both on the mass of the dark photon and the kinetic mixing strength. To that end, various experiments adjust beam energy, and shield thickness to probe different regions of parameter space. These approaches will be discussed further, with references, in part 2.

The particular work presented here focuses on another facet of the kinetic mixing scenario: as will be discussed further in part 2, in order for kinetic mixing to occur there must be an additional new particle, the "mediator", which would generate kinetic mixing by "linking" the two gauge bosons. The precise meaning of this will be clarified later on, however, for the time being it is interesting to note that in some cases, particularly *nonabelian* kinetic mixing (in which one or the other of the associated gauge fields are nonabelian), the mass of the mediating particle is directly linked to the strength of kinetic mixing. As I will show later on, this allows us to make striking predictions which link the fixed target and beam dump experiments to lepton-jet searches at particle colliders.

This dissertation includes previously published and unpublished co-authored material. The work presented in chapter 2 was done in collaboration with Christopher A. Newby and Spencer Chang and has been published in Physical Review D [20]. The model-building work in chapter 3 was done in collaboration with Christopher A. Newby and Spencer Chang and is currently under review for publication in Physical Review Letters [21]. The collider study work in chapter 3 was done in collaboration with with Christopher A. Newby, Spencer Chang, and Bryan M. Ostdiek and is ongoing.

CHAPTER II

A MODEL INDEPENDENT APPROACH TO INELASTIC DARK MATTER DIRECT DETECTION

This chapter is based on previously published, co-authored material[1].

Dark matter direct detection experiments are an ambitious effort to observe galactic dark matter scattering off of nuclear targets [22] as a means to study dark matter's interactions with normal matter. Beginning with the early experiments in the eighties, there has been steady progress to increasing sensitivity. Planned experiments in the future will push this frontier [23], giving us hope that such interactions will be confirmed soon. Such a discovery would give important insights into the fundamental nature of dark matter and its place in the Standard Model of particle physics.

The experimental challenges of direct detection are many. Finding conclusive evidence is a tall order, as demonstrated by several recent experimental anomalies, the most famous being the annual modulation signal seen by DAMA [7], which appear to be in conflict with the null results of other experiments. However, whether a dark matter scenario is consistent with existing limits and excesses depends strongly on the form of its interactions with the nucleus. For each interaction, the relative sensitivities of different experiments can vary wildly, leading to the hope of a scenario consistent with all of the existing data. Another reason to study the allowed interactions is that certain interactions may have distinctive features in the signal that allow better background separation. These reasons highlight the importance of exploring the full landscape of possible interactions. Some examples of the studied possibilities

[1]This chapter is based on reference [20] written in collaboration with Spencer Chang and Christopher A. Newby

include inelastic transitions [13], dark matter form factors [24, 25], dark matter-nucleus resonances [26, 27], and isospin-violating dark matter [28–30].

Given the large range of possible scattering interactions allowed by dark matter theories, it has proven useful to study the phenomenology of dark matter scattering in a model independent fashion [11, 31]. In particular, Ref. [11] has provided a systematic study of the effective description of nonrelativistic, elastic scattering and a Mathematica package to generate the necessary form factors [32]. A notable success of this approach was the illumination of nuclear responses beyond the standard spin-independent and spin-dependent responses that are primarily considered by dark matter experiments. Thus, model independent approaches have the benefit of larger applicability, pointing out all of the regions where experiments can be sensitive — see [33–38] for some recent work in this direction.

In this paper, we extend this work by considering the modifications necessary to describe inelastic transitions of the dark matter particle. Such transitions have important kinematic effects and were originally proposed and studied for scattering to a heavier dark matter state [13, 39] and then later extended to the "down scattering" case [40–42]. We will investigate the modifications to Ref. [11] that must be made to properly treat inelastic scattering in a model-independent fashion. As we will show, this requires a straightforward reorganization of the basis of scattering matrix-elements. This has the added benefit that we were able to suitably modify the Mathematica package [32] to calculate the form factors for inelastic scattering.

To illustrate the utility of this methodology, we will demonstrate how the inelastic transitions between particles of spin 1/2 to 1/2, 0 to 1, and 0 to 0 can be treated in a standard basis of nonrelativistic matrix elements. We do so by considering the relativistic operators between such particles that can be mediated by spin 0 or

1 particles. Using these results, we perform a reanalysis of the magnetic inelastic dark matter scenario [43] and perform a model independent scan over the relativistic operators to determine scenarios which could explain the DAMA/LIBRA signal. For the magnetic inelastic dark matter scenario and for operators which couple the dark matter to protons only, we find the constraints from xenon detectors can be weakened to allow some operators to survive, while germanium detectors have an extremely weak sensitivity. However, a stringent constraint comes from iodine targets, like those used by COUPP and KIMS. A large uncertainty in this analysis is the quenching factor of iodine. Depending on the values we assume, the constraints from KIMS, XENON, and LUX can change by a large amount, due to changes in the recoil spectra. Another uncertainty is the lack of form factors for cesium and tungsten. Given these uncertainties, we find that DAMA explanations are constrained but not ruled out yet, which should be resolved by the next round of experimental releases.

The outline of the rest of the paper is as follows. In section 2.1, we discuss the kinematics of inelastic scattering to determine the relevant kinematic variables. In section 2.2 we discuss the modifications to the operators needed to describe dark matter inelastic transitions. In section 2.3, as an application of this formalism, we fit the annual modulation signal at DAMA/LIBRA and discuss the constraints from other experiments. In section 2.4, we conclude. Finally, in the appendices, we give further details on the nonrelativistic limit of the kinematics and matrix elements of inelastic scattering.

Variables for Inelastic Kinematics

To begin, we need to determine the correct variables to describe inelastic scattering. To do so, we need to understand the kinematic modifications of an inelastic

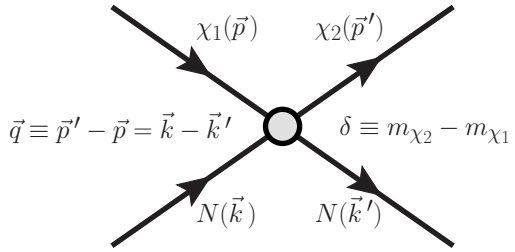

FIGURE 1. Inelastic scattering of dark matter off of a nucleon with our conventions for the kinematic variables.

transition for nonrelativistic scattering. We are interested in scattering events of the type

$$\chi_1(\vec{p})\ N(\vec{k}\,) \to \chi_2(\vec{p}\,')\ N(\vec{k}\,') \tag{2.1}$$

where χ_1 is the incoming dark matter particle, χ_2 is the outgoing particle, and N is a nucleon in the target nucleus, see Fig. 1. There is a mass splitting between the two particles $\delta = m_{\chi_2} - m_{\chi_1}$. Positive δ was the first case to be considered originally [13], which pointed out that this has the important effects of favoring scattering off of heavier nuclei and increasing the annual modulation fraction. Negative δ leads to exothermic transitions which have also been considered in the literature [40–42]. In certain theories, the elastic scattering process is forbidden or suppressed [44, 45], making these inelastic transitions the leading way to detect dark matter scattering. For a survey of such theories, see [13, 46–50].

The modifications of a nonzero splitting δ on the kinematics is straightforward. To leading order in the nonrelativistic expansion, δ is the additional energy required to make the transition occur. Thus, given the scaling of kinetic energy, we expect situations where the splitting scales as $\delta \sim O(v^2)$ to have a consistent velocity

expansion. Since dark matter in our galaxy have speeds $v \sim 10^{-3}c$, this means that we should consider splittings in the range $\delta \sim 100$ keV $\left(\frac{m_\chi}{100 \text{ GeV}}\right)$.

Now, we adapt the analysis of [11] to inelastic scattering in order to determine the relevant degrees of freedom that characterize the effective theory in a velocity expansion. One approach would be to start with the relativistic kinematics and take the nonrelativistic limit. Although this gives the same result, as we show in Appendix **??**, we find that it is simpler to proceed from the constraints of Galilean invariance where velocities receive a common shift. This determines that there are two relevant vectors that are boost invariant, $\vec{v} \equiv \vec{v}_{\chi_1} - \vec{v}_{N_{in}} = \vec{p}/m_{\chi_1} - \vec{k}/m_N$ and $\vec{q} = \vec{p}\,' - \vec{p} = \vec{k} - \vec{k}'$, while the boost invariant scalars are the particle masses and δ. Note that $\vec{p}\,' - \vec{p}$ is not exactly Galilean invariant; due to the mass difference δ, it is invariant to leading order in the velocity expansion and thus is a consistent approximation at first order. Throughout this discussion, we are working in this expansion and will cavalierly use equalities for expressions if they are equal to the same order in the expansion.

At this point, it is useful to construct an orthogonal basis of these vectors. To do so, consider the scattering in the center-of-mass frame, where $\vec{v}_{\chi_1} = \frac{\mu_N}{m_{\chi_1}}\vec{v}$, $\vec{v}_{N_{in}} = -\frac{\mu_N}{m_N}\vec{v}$, and μ_N is the reduced mass between χ_1 and N. The initial energy in this frame, expanded to second order in velocities, is

$$E_{in} \approx m_{\chi_1} + m_N + \frac{1}{2}\mu_N v^2. \tag{2.2}$$

After scattering, the momentum vectors are $\vec{p}' = \vec{p} + \vec{q}$ and $\vec{k}' = \vec{k} - \vec{q}$. Expanding the final energy to the same order, we find

$$\begin{aligned} E_{out} &= m_{\chi_2} + m_N + \frac{1}{2m_{\chi_2}}|\vec{p} + \vec{q}|^2 + \frac{1}{2m_N}|\vec{k} - \vec{q}|^2 \\ &\approx E_{in} + \delta + \vec{v} \cdot \vec{q} + \frac{|\vec{q}|^2}{2\mu_N}. \end{aligned} \tag{2.3}$$

To reach the final form, we treated all momenta as order v and δ as order v^2. Thus, we find that energy conservation requires

$$\delta + \vec{v} \cdot \vec{q} + \frac{|\vec{q}|^2}{2\mu_N} = 0. \tag{2.4}$$

Using this constraint, one can easily show that

$$\vec{v}^{\perp}_{\text{inel}} \equiv \vec{v} + \frac{\vec{q}}{2\mu_N} + \frac{\delta}{|\vec{q}|^2}\vec{q} = \vec{v}^{\perp}_{\text{el}} + \frac{\delta}{|\vec{q}|^2}\vec{q} \tag{2.5}$$

is perpendicular to $\vec{q}$. Here we see that the inelastic kinematics alters this vector from the elastic version $\vec{v}^{\perp}_{\text{el}}$ by a new piece proportional to δ. This new term is entirely consistent with the velocity expansion.

As a consistency check, notice that Eq. 2.4 requires

$$|\vec{v}| \geq \frac{1}{|\vec{q}|}\left|\frac{|\vec{q}|^2}{2\mu_N} + \delta\right|. \tag{2.6}$$

If we write the momentum transfer in terms of the energy recoil $|\vec{q}| = \sqrt{2m_N E_R}$, we find that the minimum velocity for scattering is

$$v_{\text{min}} = \frac{1}{\sqrt{2m_N E_R}}\left|\frac{m_N E_R}{\mu_N} + \delta\right| \tag{2.7}$$

which reproduces the well known result in the literature [13].

Inelastic Scattering Operators

Now that we know the correct variables to describe inelastic kinematics, we can list the allowed matrix elements for inelastic, nonrelativistic dark matter-nucleon scattering. To leading order in the velocity expansion, we found that the only modification is that $\vec{v}^{\perp}$ is changed from the elastic case. Thus, the operators that are allowed are the same as in [11] with $\vec{v}^{\perp} \to \vec{v}^{\perp}_{\text{inel}}$. Listing these in the same numbering scheme, we have

$$
\begin{aligned}
&\mathcal{O}_1 = \mathbf{1}_\chi \mathbf{1}_N, \quad \mathcal{O}_2 = (v^{\perp}_{\text{inel}})^2, \quad \mathcal{O}_3 = i\vec{S}_N \cdot \left(\frac{\vec{q}}{m_N} \times \vec{v}^{\perp}_{\text{inel}} \right), \\
&\mathcal{O}_4 = \vec{S}_\chi \cdot \vec{S}_N, \quad \mathcal{O}_5 = i\vec{S}_\chi \cdot \left(\frac{\vec{q}}{m_N} \times \vec{v}^{\perp}_{\text{inel}} \right), \\
&\mathcal{O}_6 = \left(\vec{S}_\chi \cdot \frac{\vec{q}}{m_N} \right) \left(\vec{S}_N \cdot \frac{\vec{q}}{m_N} \right), \\
&\mathcal{O}_7 = \vec{S}_N \cdot \vec{v}^{\perp}_{\text{inel}}, \quad \mathcal{O}_8 = \vec{S}_\chi \cdot \vec{v}^{\perp}_{\text{inel}}, \\
&\mathcal{O}_9 = i\vec{S}_\chi \cdot \left(\vec{S}_N \times \frac{\vec{q}}{m_N} \right), \quad \mathcal{O}_{10} = i\vec{S}_N \cdot \frac{\vec{q}}{m_N}, \\
&\mathcal{O}_{11} = i\vec{S}_\chi \cdot \frac{\vec{q}}{m_N}, \quad \mathcal{O}_{12} = \vec{S}_\chi \cdot \left(\vec{S}_N \times \vec{v}^{\perp}_{\text{inel}} \right), \\
&\mathcal{O}_{13} = i \left(\vec{S}_\chi \cdot \vec{v}^{\perp}_{\text{inel}} \right) \left(\vec{S}_N \cdot \frac{\vec{q}}{m_N} \right), \\
&\mathcal{O}_{14} = i \left(\vec{S}_\chi \cdot \frac{\vec{q}}{m_N} \right) \left(\vec{S}_N \cdot \vec{v}^{\perp}_{\text{inel}} \right), \\
&\mathcal{O}_{15} = - \left(\vec{S}_\chi \cdot \frac{\vec{q}}{m_N} \right) \left((\vec{S}_N \times \vec{v}^{\perp}_{\text{inel}}) \cdot \frac{\vec{q}}{m_N} \right),
\end{aligned}
\tag{2.8}
$$

where $\vec{S}_{\chi,N}$ are the spin operators for the dark matter and nucleon. In [11], operator $\mathcal{O}_2$ was not considered since it doesn't appear in the nonrelativistic reduction of the scattering matrix elements of relativistic operators, and we find the same result here.

Thus, the important operators are at most linear in $\vec{v}^{\perp}_{\text{inel}}$. Since $\vec{v}^{\perp}_{\text{inel}}$ differs from the elastic $\vec{v}^{\perp}$ by just a shift in $\vec{q}$, we will later find that this linearity allows one to utilize the form factors provided by the Mathematica package [32].

There are two other modifications to the elastic case that we will find. First of all, δ can be a coefficient multiplying the operators when one reduces from relativistic operators. The second effect is that $\vec{q}$ no longer has to appear in the combination of $i\vec{q}$, as can be seen by the expression for $\vec{v}^{\perp}_{\text{inel}}$. In the elastic case, this was guaranteed by the interaction being Hermitian. Since conjugation swaps initial and final states, this acts as time reversal, $i\vec{q} \xrightarrow{T} i\vec{q}$. However, for the inelastic case, the initial and final states are not the same particle, so this is no longer required by the interaction. In general, the inelastic operators in Eq. 2.8 may have arbitrary complex coefficients, as long as they appear in appropriate Hermitian conjugate pairs in the Hamiltonian. This was not the case for elastic operators because Hermiticity requires them to have real coefficients.

Form Factors for Inelastic Scattering

Now, one must use these nucleon-dark matter operators to determine the matrix elements within the target nucleus. We will give a brief summary here, giving more details in Appendix **??**. Since inelasticity modifies $\vec{v}^{\perp}_{\text{inel}}$, we should examine how this affects the nuclear response. First of all, by introducing the target velocity $\vec{v}_T$, we

rewrite

$$\begin{aligned}
\vec{v}_{\rm el}^{\perp} &= \vec{v} + \frac{\vec{q}}{2\mu_N} \\
&= \left(\frac{\vec{p}}{m_{\chi_1}} - \frac{\vec{k}}{m_N}\right) + \frac{1}{2m_{\chi_1}}\left(\vec{p}' - \vec{p}\right) + \frac{1}{2m_N}\left(\vec{k} - \vec{k}'\right) \\
&\approx \frac{1}{2}(\vec{v}_{\chi_1} + \vec{v}_{\chi_2} - \vec{v}_{N_{in}} - \vec{v}_{N_{out}}) \\
&= \frac{1}{2}(\vec{v}_{\chi_1} + \vec{v}_{\chi_2} - \vec{v}_{T_{in}} - \vec{v}_{T_{out}}) \\
&\quad + \frac{1}{2}\left[(\vec{v}_{T_{in}} - \vec{v}_{N_{in}}) + (\vec{v}_{T_{out}} - \vec{v}_{N_{out}})\right] \\
&\equiv \vec{v}_{{\rm el}\,T}^{\perp} + \vec{v}_{\rm nuc}.
\end{aligned} \tag{2.9}$$

Thus for each nucleon in the nucleus, $\vec{v}_{\rm el}^{\perp}$ is equal to the target's $\vec{v}_{\rm el}^{\perp}$ plus a term, $\vec{v}_{\rm nuc}$, that is dependent on the nucleon's relative velocity to the nucleus. Similarly, for the inelastic velocity, we have

$$\vec{v}_{\rm inel}^{\perp} = \vec{v}_{{\rm inel}\,T}^{\perp} + \vec{v}_{\rm nuc} \tag{2.10}$$

where

$$\vec{v}_{{\rm inel}\,T}^{\perp} = \frac{1}{2}(\vec{v}_{\chi_1} + \vec{v}_{\chi_2} - \vec{v}_{T_{in}} - \vec{v}_{T_{out}}) + \frac{\delta}{|\vec{q}|^2}\vec{q}, \tag{2.11}$$

Since the nucleus and dark matter scattering is also in the nonrelativistic limit, the same kinematic considerations from before show that $\vec{v}_{{\rm inel}\,T}^{\perp}$ is perpendicular to $\vec{q}$ and thus we can now interpret $\vec{q}$ as the momentum transfer from χ_1 to the target *nucleus*.

The reason for the separation of $\vec{v}_{{\rm inel}\,T}^{\perp}$ into target and relative parts is that the nuclear form-factors only depend on interactions with *nucleons*, so only $\vec{v}_{\rm nuc}$ is an operator. The five nucleon interactions are [11]:

$$\begin{aligned}
&\mathcal{O}_1^N = \mathbf{1}_N, \qquad \mathcal{O}_2^N = -2\vec{v}_{\rm nuc}\cdot\vec{S}_N, \\
&\vec{\mathcal{O}}_3^N = 2\vec{S}_N, \qquad \vec{\mathcal{O}}_4^N = -\vec{v}_{\rm nuc}, \text{ and} \\
&\vec{\mathcal{O}}_5^N = 2i\vec{v}_{\rm nuc}\times\vec{S}_N.
\end{aligned} \tag{2.12}$$

which correspond to different types of nucleon responses. $\mathcal{O}_1^N$ corresponds to the charge interaction, $\mathcal{O}_2^N$ to the axial charge interaction, $\vec{\mathcal{O}}_3^N$ to the axial vector interaction, $\vec{\mathcal{O}}_4^N$ to the vector magnetic interaction, and $\vec{\mathcal{O}}_5^N$ to the vector electric interaction. Note that the explicit dependence on the inelastic nature of the scattering is not in the operators but in the coefficients. For a more detailed discussion of the nuclear form factors see [11].

For our cases, since $\vec{v}_{\rm inel}^{\perp}$ only appears linearly (see Tables 1-3), we merely have to incorporate the change of $\vec{v}_{{\rm el}\,T}^{\perp} \to \vec{v}_{{\rm inel}\,T}^{\perp}$ in the Mathematica notebook [32]. In calculating the matrix elements squared, this results in terms which are proportional to $|\vec{v}_{{\rm inel}\,T}^{\perp}|^2$. This has the simple form

$$\begin{aligned}
|\vec{v}_{{\rm inel}\,T}^{\perp}|^2 &= |\vec{v}_T|^2 - \left(\frac{1}{2\mu_T} + \frac{\delta}{|\vec{q}|^2}\right)^2 |\vec{q}|^2 \\
&= |\vec{v}_T|^2 - v_{{\rm min}\,T}^2
\end{aligned} \tag{2.13}$$

where $\vec{v}_T = \vec{v}_{\chi_1} - \vec{v}_{T_{in}}$ and μ_T is the χ_1-nucleus reduced mass. In the second form, we have written the subtracted term as $v_{{\rm min}\,T}$, the minimum speed to scatter off of the nucleus with energy E_R, which is the nucleus version of Eq. 2.7. Note that for upscattering ($\delta > 0$) this leads to a suppression of this factor and for both signs of δ, this term goes to zero at the minimum incoming velocity.

The power of this formalism is that it gives the correct variables in which to characterize inelastic scattering and thus is helpful for understanding results that are at first surprising. As an example, in Ref. [43], an inelastic dark matter model was analyzed that had a magnetic dipole interaction with the nucleus. For the scattering of this dark matter dipole off of the nucleus charge, peculiar terms involving $\delta/|\vec{v}|^2, \delta/E_R$ are found. In that paper, these terms were only discovered by a systematic expansion. However, in terms of this discussion, these terms are just due to the contribution from the δ dependent terms of $|\vec{v}^{\perp}_{\text{inel}\,T}|^2$. Of course, the main improvement on Ref. [43] is that the form factors can now be reliably computed by a modification of the Mathematica notebook [32]. Again, for details on how to implement these inelastic modifications to the form factor calculation, see Appendix **??**.

Relativistic Matrix Elements for Fermion-Fermion Inelastic Transitions

As a first application of this formalism, let's analyze the case where $\chi_{1,2}$ are both spin 1/2 fermions. We start with the relativistic operators that would generate such scattering off of a nucleon. We list the same twenty operators of [32] in Table 1 for inelastic scattering [2]. Factors of $1/m_M$ are added to get the correct mass dimension, where m_M is a proxy for the mass of the mediator for the interaction. This coefficient involves powers of the UV coupling strength and can have strong q^2 dependence, especially if the mediator is light or massless. Factors of i are set up so that if $\Psi_2 = \Psi_1$, the operator is Hermitian, thus allowing a convenient comparison to the elastic case by taking $\delta = 0$. The third column is the nonrelativistic limit of the matrix element after multiplying by $1/(4m_N m_\chi)$ to get to standard nonrelativistic

[2] Our operator 20 has one less factor of i due to a typo in [32].

normalization. This matrix element is then decomposed in the final column in the basis of the fifteen nonrelativistic operators of Eq. 2.8.

When calculating the matrix elements, we do not find explicit terms with $\vec{v}^{\perp}_{\rm inel}$, instead we get terms of $\vec{v}^{\perp}_{\rm el}$. This is because the additional term of $\frac{\delta}{|\vec{q}|^2}\vec{q}$ does not appear in the nonrelativistic reduction. However, many factors of $\vec{v}^{\perp}_{\rm el}$ appear as $\vec{v}^{\perp}_{\rm el}\cdot(\vec{q}\times\vec{S})$ which are equivalent to $\vec{v}^{\perp}_{\rm inel}\cdot(\vec{q}\times\vec{S})$. The other terms are of the form $\vec{v}^{\perp}_{\rm el}\cdot\vec{S}$ which we rewrite as $(\vec{v}^{\perp}_{\rm inel}-\frac{\delta}{|\vec{q}|^2}\vec{q})\cdot\vec{S}$. Writing the matrix elements in terms of $\vec{v}^{\perp}_{\rm inel}$ is convenient since it minimizes cross terms in the matrix element squared. Note that in operators 18 and 19 there are additional terms proportional to δ which are new nontrivial contributions to the scattering amplitude. Amusingly, these contributions come from terms of $\frac{\delta}{|\vec{q}|^2}\vec{q}$ dotted into $\vec{q}$, canceling the $|\vec{q}|^2$ term in the denominator. As a final check, we see that when we take $\delta = 0$ we recover the elastic results in [32].

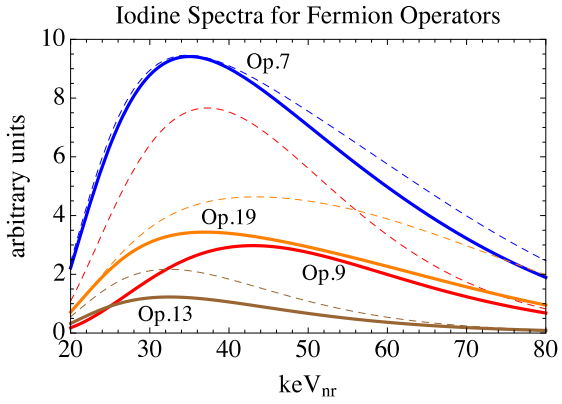

FIGURE 2. Sample iodine scattering spectra with equal couplings to protons and neutrons for fermion operators $7, 9, 13, 19$. The dark matter parameters are $m_\chi = 70$ GeV and $\delta = 120$ keV. In solid are our predicted curves while dashed curves show incorrect spectra from combining elastic form factors with the inelastic velocity threshold.

In Fig. 2, we plot some examples for the energy recoil spectra for these fermion operators in arbitrary units. In this figure, we are assuming iodine scattering with

Index	Relativistic Operator	Nonrelativistic Limit $\times \frac{1}{4m_N m_\chi}$	$\sum_i c_i \mathcal{O}_i$
1	$\bar{\chi}_2\chi_1\bar{N}N$	$\mathbf{1}_\chi \mathbf{1}_N$	$\mathcal{O}_1$
2	$i\bar{\chi}_2\chi_1\bar{N}\gamma^5 N$	$i\frac{\vec{q}}{m_N}\cdot\vec{S}_N$	$\mathcal{O}_{10}$
3	$i\bar{\chi}_2\gamma^5\chi_1\bar{N}N$	$-i\frac{\vec{q}}{m_\chi}\cdot\vec{S}_\chi$	$-\frac{m_N}{m_\chi}\mathcal{O}_{11}$
4	$\bar{\chi}_2\gamma^5\chi_1\bar{N}\gamma^5 N$	$-(\frac{\vec{q}}{m_\chi}\cdot\vec{S}_\chi)(\frac{\vec{q}}{m_N}\cdot\vec{S}_N)$	$-\frac{m_N}{m_\chi}\mathcal{O}_6$
5	$\bar{\chi}_2\gamma^\mu\chi_1\bar{N}\gamma_\mu N$	$\mathbf{1}_\chi \mathbf{1}_N$	$\mathcal{O}_1$
6	$\bar{\chi}_2\gamma^\mu\chi_1\bar{N}i\sigma_{\mu\nu}\frac{q^\nu}{m_M}N$	$\frac{\vec{\lvert q\rvert}^2}{2m_N m_M}\mathbf{1}_\chi\mathbf{1}_N$ $+2\left(\frac{\vec{q}}{m_\chi}\times\vec{S}_\chi+i\vec{v}^\perp_{\rm inel}\right)\cdot\left(\frac{\vec{q}}{m_M}\times\vec{S}_N\right)$	$\frac{\vec{\lvert q\rvert}^2}{2m_N m_M}\left(\mathcal{O}_1+\frac{4m_N}{m_\chi}\mathcal{O}_4\right)$ $-\frac{2m_N}{m_M}\left(\frac{m_N}{m_\chi}\mathcal{O}_6+\mathcal{O}_3\right)$
7	$\bar{\chi}_2\gamma^\mu\chi_1\bar{N}\gamma_\mu\gamma^5 N$	$-2\vec{S}_N\cdot(\vec{v}^\perp_{\rm inel}-\frac{\delta}{\vec{\lvert q\rvert}^2}\vec{q})$ $+2i\vec{S}_\chi\cdot(\vec{S}_N\times\frac{\vec{q}}{m_\chi})$	$-2\left(\mathcal{O}_7+i\frac{m_N\delta}{\vec{\lvert q\rvert}^2}\mathcal{O}_{10}-\frac{m_N}{m_\chi}\mathcal{O}_9\right)$
8	$i\bar{\chi}_2\gamma^\mu\chi_1\bar{N}i\sigma_{\mu\nu}\frac{q^\nu}{m_M}\gamma^5 N$	$2i\frac{\vec{q}}{m_M}\cdot\vec{S}_N$	$\frac{2m_N}{m_M}\mathcal{O}_{10}$
9	$\bar{\chi}_2 i\sigma^{\mu\nu}\frac{q_\nu}{m_M}\chi_1\bar{N}\gamma_\mu N$	$-\frac{\vec{\lvert q\rvert}^2}{2m_\chi m_M}\mathbf{1}_\chi\mathbf{1}_N$ $-2\left(\frac{\vec{q}}{m_N}\times\vec{S}_N+i\vec{v}^\perp_{\rm inel}\right)\cdot\left(\frac{\vec{q}}{m_M}\times\vec{S}_\chi\right)$	$-\frac{\vec{\lvert q\rvert}^2}{2m_\chi m_M}\left(\mathcal{O}_1+\frac{4m_\chi}{m_N}\mathcal{O}_4\right)$ $+\frac{2m_N}{m_M}\left(\mathcal{O}_6+\mathcal{O}_5\right)$
10	$\bar{\chi}_2 i\sigma^{\mu\nu}\frac{q_\nu}{m_M}\chi_1\bar{N}i\sigma_{\mu\alpha}\frac{q^\alpha}{m_M}N$	$4\left(\frac{\vec{q}}{m_M}\times\vec{S}_\chi\right)\cdot\left(\frac{\vec{q}}{m_M}\times\vec{S}_N\right)$	$\frac{4m_N^2}{m_M^2}\left(\frac{\vec{\lvert q\rvert}^2}{m_N^2}\mathcal{O}_4-\mathcal{O}_6\right)$

TABLE 1. Relativistic operators for inelastic transitions between two fermions $\chi_{1,2}$, their matrix element in the nonrelativistic limit multiplied by a factor of $1/(4m_\chi m_N)$, and their expansion in the basis of allowed scattering matrix-elements.

11	$\bar{\chi}_2 i\sigma^{\mu\nu}\frac{q_\nu}{m_M}\chi_1\bar{N}\gamma_\mu\gamma^5 N$	$4i\left(\frac{\vec{q}}{m_M}\times\vec{S}_\chi\right)\cdot\vec{S}_N$	$\frac{4m_N}{m_M}\mathcal{O}_9$
12	$i\bar{\chi}_2 i\sigma^{\mu\nu}\frac{q_\nu}{m_M}\chi_1\bar{N}i\sigma_{\mu\alpha}\frac{q^\alpha}{m_M}\gamma^5 N$	$-\left[i\frac{\vec{\lvert q\rvert}^2}{m_\chi m_M}-4\vec{v}^\perp_{\rm inel}\cdot\left(\frac{\vec{q}}{m_M}\times\vec{S}_\chi\right)\right]\frac{\vec{q}}{m_M}\cdot\vec{S}_N$	$-\frac{\vec{\lvert q\rvert}^2}{m_M^2}\left(\frac{m_N}{m_\chi}\mathcal{O}_{10}+4\mathcal{O}_{12}\right)$ $-\frac{4m_N^2}{m_M^2}\mathcal{O}_{15}$
13	$\bar{\chi}_2\gamma^\mu\gamma^5\chi_1\bar{N}\gamma_\mu N$	$2\left(\vec{v}^\perp_{\rm inel}-\frac{\delta}{\vec{\lvert q\rvert}^2}\vec{q}\right)\cdot\vec{S}_\chi$ $+2i\vec{S}_\chi\cdot\left(\vec{S}_N\times\frac{\vec{q}}{m_N}\right)$	$2\left(\mathcal{O}_8+\mathcal{O}_9+i\frac{m_N\delta}{\vec{\lvert q\rvert}^2}\mathcal{O}_{11}\right)$
14	$\bar{\chi}_2\gamma^\mu\gamma^5\chi_1\bar{N}i\sigma_{\mu\nu}\frac{q^\nu}{m_M}N$	$4i\vec{S}_\chi\cdot\left(\frac{\vec{q}}{m_M}\times\vec{S}_N\right)$	$-\frac{4m_N}{m_M}\mathcal{O}_9$
15	$\bar{\chi}_2\gamma^\mu\gamma^5\chi_1\bar{N}\gamma_\mu\gamma^5 N$	$-4\vec{S}_\chi\cdot\vec{S}_N$	$-4\mathcal{O}_4$
16	$i\bar{\chi}_2\gamma^\mu\gamma^5\chi_1\bar{N}i\sigma_{\mu\nu}\frac{q^\nu}{m_M}\gamma^5 N$	$4i\frac{\vec{q}}{m_M}\cdot\vec{S}_N\left(\vec{v}^\perp_{\rm inel}-\frac{\delta}{\vec{\lvert q\rvert}^2}\vec{q}\right)\cdot\vec{S}_\chi$	$\frac{4m_N}{m_M}\left(\mathcal{O}_{13}-i\frac{m_N\delta}{\vec{\lvert q\rvert}^2}\mathcal{O}_6\right)$
17	$i\bar{\chi}_2 i\sigma^{\mu\nu}\frac{q_\nu}{m_M}\gamma^5\chi_1\bar{N}\gamma_\mu N$	$2i\frac{\vec{q}}{m_M}\cdot\vec{S}_\chi$	$\frac{2m_N}{m_M}\mathcal{O}_{11}$
18	$i\bar{\chi}_2 i\sigma^{\mu\nu}\frac{q_\nu}{m_M}\gamma^5\chi_1\bar{N}i\sigma_{\mu\alpha}\frac{q^\alpha}{m_M}N$	$\vec{S}_\chi\cdot\frac{\vec{q}}{m_M}\left[i\frac{\vec{\lvert q\rvert}^2}{m_N m_M}-4\vec{v}^\perp_{\rm inel}\cdot(\frac{\vec{q}}{m_M}\times\vec{S}_N)\right]$ $-4\frac{\delta}{m_M}\vec{S}_\chi\cdot(\frac{\vec{q}}{m_M}\times\vec{S}_N)$	$\frac{m_N^2}{m_M^2}\left(\frac{\vec{\lvert q\rvert}^2}{m_N^2}\mathcal{O}_{11}+4\mathcal{O}_{15}\right)$ $-i\frac{4m_N\delta}{m_M^2}\mathcal{O}_9$
19	$i\bar{\chi}_2 i\sigma^{\mu\nu}\frac{q_\nu}{m_M}\gamma^5\chi_1\bar{N}\gamma_\mu\gamma^5 N$	$-4i\frac{\vec{q}}{m_M}\cdot\vec{S}_\chi\left(\vec{v}^\perp_{\rm inel}-\frac{\delta}{\vec{\lvert q\rvert}^2}\vec{q}\right)\cdot\vec{S}_N$ $-i\frac{4\delta}{m_M}\vec{S}_\chi\cdot\vec{S}_N$	$-\frac{4m_N}{m_M}\left(\mathcal{O}_{14}-i\frac{m_N\delta}{\vec{\lvert q\rvert}^2}\mathcal{O}_6\right)$ $-i\frac{4\delta}{m_M}\mathcal{O}_4$
20	$\bar{\chi}_2 i\sigma^{\mu\nu}\frac{q_\nu}{m_M}\gamma^5\chi_1\bar{N}i\sigma_{\mu\alpha}\frac{q^\alpha}{m_M}\gamma^5 N$	$4\frac{\vec{q}}{m_M}\cdot\vec{S}_\chi\frac{\vec{q}}{m_M}\cdot\vec{S}_N$	$\frac{4m_N^2}{m_M^2}\mathcal{O}_6$

equal couplings to protons and neutrons with a dark matter mass $m_\chi = 70$ GeV and mass splitting $\delta = 120$ keV. In solid lines, we have our predicted rates. As a comparison, we show in dashed lines an incorrect spectra if we had taken the elastic form factors but still integrated from the correct minimum velocity for inelastic scattering, $v_{\min T}$. Notice that the correct spectra is always smaller than the incorrect spectra for the operators considered with a positive δ. This reflects the vanishing of $|\vec{v}^{\perp}_{\text{inel}\,T}|^2$ on threshold. We chose these operators (7, 9, 13, 19) because they illustrate that the inelastic modifications to the form factors can in some cases significantly alter the shape and normalization of the spectra. In addition, we found these differences to be quite sensitive to the choice of target nuclei and isospin structure of the nucleon couplings.

Relativistic Matrix Elements for Scalar-Vector Inelastic Transitions

An additional novelty of inelastic scattering is that it allows transitions between dark matter particles of different spin. In this section, we consider the case where this transition is between a scalar Φ and a vector V^μ. Such nearly degenerate states have been shown to occur in models where the dark matter is composite [47, 48] due to a hyperfine splitting in the dark sector. In Table 2, we list eight Hermitian operators which can be mediated by either spin 0 or 1 mediators. For the third column, we list the matrix element's nonrelativistic limit after multiplying by a factor of $1/(2m_N)$ to go to the standard nonrelativistic normalization for the nucleons.

All of these matrix elements are in the form of $M = \vec{X} \cdot \vec{\epsilon}$, where $\vec{\epsilon}$ is the polarization vector of the spin 1 dark matter particle (which we take to be real for notational simplicity). Depending on whether the spin 1 particle is in the initial or final state, we have to average or sum over these polarizations. Since $\sum_{pol} \epsilon^i \epsilon^j = \delta^{ij}$,

Index	Relativistic Operator	Nonrelativistic Limit $\times\frac{1}{2m_N}$	$\sum_i c_i\mathcal{O}_i$
1	$\frac{1}{m_M}\left(\Phi\overleftrightarrow{\partial}_\mu V^\mu\right)\bar{N}N$	$i\frac{\vec{q}}{m_M}\cdot\vec{\varepsilon}$	$\frac{m_N}{m_M}\mathcal{O}_{11}$
2	$\frac{1}{m_M}\partial_\mu(\Phi V^\mu)\,\bar{N}N$	$i\frac{\vec{q}}{m_M}\cdot\vec{\varepsilon}$	$\frac{m_N}{m_M}\mathcal{O}_{11}$
3	$\Phi V^\mu\bar{N}\gamma_\mu N$	$\frac{1}{2}\vec{\varepsilon}\cdot\left[2\vec{v}_{\rm inel}^{\perp}-\left(\frac{2m_N\delta}{\lvert\vec{q}\rvert^2}-\frac{m_N}{m_\chi}\right)\frac{\vec{q}}{m_N}\right]-i\vec{\varepsilon}\cdot(\frac{\vec{q}}{m_N}\times\vec{S}_N)$	$\mathcal{O}_8-\mathcal{O}_9+\frac{i}{2}\left(\frac{2m_N\delta}{\lvert\vec{q}\rvert^2}-\frac{m_N}{m_\chi}\right)\mathcal{O}_{11}$
4	$\frac{i}{m_M}\left(\Phi\overleftrightarrow{\partial}_\mu V^\mu\right)\bar{N}\gamma^5N$	$-\frac{\vec{q}}{m_M}\cdot\vec{\varepsilon}\frac{\vec{q}}{m_N}\cdot\vec{S}_N$	$-\frac{m_N}{m_M}\mathcal{O}_6$
5	$\frac{i}{m_M}\partial_\mu(\Phi V^\mu)\,\bar{N}\gamma^5N$	$-\frac{\vec{q}}{m_M}\cdot\vec{\varepsilon}\frac{\vec{q}}{m_N}\cdot\vec{S}_N$	$-\frac{m_N}{m_M}\mathcal{O}_6$
6	$\Phi V^\mu\bar{N}\gamma_\mu\gamma^5N$	$-2\vec{S}_N\cdot\vec{\varepsilon}$	$-2\mathcal{O}_4$
7	$\Phi V^\mu\bar{N}i\sigma_{\mu\nu}\frac{q^\nu}{m_M}N$	$2i\vec{\varepsilon}\cdot(\frac{\vec{q}}{m_M}\times\vec{S}_N)$	$-2\frac{m_N}{m_M}\mathcal{O}_9$
8	$i\Phi V^\mu\bar{N}i\sigma_{\mu\nu}\frac{q^\nu}{m_M}\gamma^5N$	$i\vec{\varepsilon}\cdot\left[2\vec{v}_{\rm inel}^{\perp}-\left(\frac{2m_N\delta}{\lvert\vec{q}\rvert^2}-\frac{m_N}{m_\chi}\right)\frac{\vec{q}}{m_N}\right]\frac{\vec{q}}{m_M}\cdot\vec{S}_N$	$\frac{m_N}{m_M}\left[2\mathcal{O}_{13}-i\left(\frac{2m_N\delta}{\lvert\vec{q}\rvert^2}-\frac{m_N}{m_\chi}\right)\mathcal{O}_6\right]$

TABLE 2. The inelastic relativistic operators for a transition from a dark matter particle of spin 0 to a spin 1 particle, $\Phi\to V^\mu$, their matrix element in the nonrelativistic limit after multiplying by a factor of $1/(2m_N)$, and then their decomposition in the basis of allowed scattering matrix elements. This final step of replacing the spin 1 polarization vector $\vec{\epsilon}$ with $\vec{S}_\chi$, is valid if we multiply the final matrix element squared by a correction factor c_{corr} in Eq. 2.16.

we have for the spin-summed (or averaged) matrix element squared

$$\overline{|M|^2} = \begin{cases} \frac{1}{3}|\vec{X}|^2 \text{ spin 1 in initial state} \\ \\ |\vec{X}|^2 \text{ spin 1 in final state} \end{cases} . \tag{2.14}$$

This form allows us to treat these matrix elements with our basis of nonrelativistic operators in the following way. If we just naively replace $\vec{\epsilon}$ with $\vec{S}_\chi$, we would have

$$\overline{|M|^2} = \frac{1}{2s_\chi + 1} \sum_{spins,i,j} S_\chi^i S_\chi^j X^{i*} X^j = \frac{s_\chi(s_\chi+1)}{3}|\vec{X}|^2. \tag{2.15}$$

Thus, we can use the same operator basis where we naively replace $\vec{\epsilon}$ with $\vec{S}_\chi$ by multiplying the final result by a correction factor

$$c_{corr} = \begin{cases} \frac{1}{s_\chi(s_\chi+1)} \text{ spin 1 in initial state} \\ \\ \frac{3}{s_\chi(s_\chi+1)} \text{ spin 1 in final state} \end{cases} . \tag{2.16}$$

Thus, in the final column of Table 2, we decompose the matrix element under this replacement of $\vec{\epsilon} \to \vec{S}_\chi$, so that we can write it in the same operator basis as the fermion case. These correction factors are accounted for in the additions we made to the Mathematica package of [32].

Relativistic Matrix Elements for Scalar-Scalar Inelastic Transitions

As one more example, we analyze the case of a dark matter scattering process with a transition from a spin 0 particle Φ_1 to another spin 0 particle Φ_2. In Table 3, we

list seven operators between these two scalars which can be mediated by either spin 0 or 1 mediators. For the third column, we list the matrix element's nonrelativistic limit after multiplying by a factor of $1/(2m_N)$ to go to the standard nonrelativistic normalization for the nucleons.

Fitting DAMA/LIBRA's annual modulation signal

In this section we present fits to the DAMA/LIBRA annual modulation signal [7]. For the following analysis we consider $\delta > 0$, which favors dark matter scattering off of heavier targets. Thus we specifically consider constraints from XENON10 [51], XENON100 [52], LUX [53], CDMS [54], COUPP [55], and KIMS [56]. Unfortunately, we cannot be inclusive in our consideration of constraints. In particular we cannot derive limits from other direct detection experiments such as CRESST ($CaWO_4$) [57] or fully analyze KIMS (CsI) which could be sensitive to the preferred parameter spaces. This is because tungsten and cesium form factors are not yet available in the Mathematica package [32], so we cannot treat them at the same level. However, KIMS most recent analysis [56] claims any scenario involving iodine scattering to explain the DAMA modulation is incompatible with their data, which considering *only* iodine scattering, is mostly accurate, but there are some exceptions. As we will demonstrate, KIMS limits are strongly dependent on the iodine quenching factors which have some large uncertainties at the moment. Given all of these caveats, we will find some allowed regions on parameter space but expect these scenarios to be tested in the near future.

Index	Relativistic Operator	Nonrelativistic Limit $\times\frac{1}{2m_N}$	$\sum_i c_i\mathcal{O}_i$
1	$\Phi_2\Phi_1\bar{N}N$	$\mathbf{1}_\chi\mathbf{1}_N$	$\mathcal{O}_1$
2	$\Phi_2\Phi_1 i\bar{N}\gamma^5 N$	$i\frac{\vec{q}}{m_N}\cdot\vec{S}_N$	$\mathcal{O}_{10}$
3	$\frac{1}{m_M}\left(i\Phi_2\overset{\leftrightarrow}{\partial}_\mu\Phi_1\right)\bar{N}\gamma^\mu N$	$2\frac{m_\chi}{m_M}\mathbf{1}_\chi\mathbf{1}_N$	$2\frac{m_\chi}{m_M}\mathcal{O}_1$
4	$\frac{1}{m_M}\left(i\Phi_2\overset{\leftrightarrow}{\partial}_\mu\Phi_1\right)\bar{N}\gamma^\mu\gamma^5 N$	$-4\frac{m_\chi}{m_M}\left(\vec{v}^\perp_{\rm inel}-\frac{\delta}{\vert\vec{q}\vert^2}\vec{q}\right)\cdot\vec{S}_N$	$-4\frac{m_\chi}{m_M}\left(\mathcal{O}_7+i\frac{m_N\delta}{\vert\vec{q}\vert^2}\mathcal{O}_{10}\right)$
5	$\frac{1}{m_M}\partial_\mu(\Phi_2\Phi_1)\,\bar{N}\gamma^\mu\gamma^5 N$	$-\frac{2i}{m_M}\vec{q}\cdot\vec{S}_N$	$-2\frac{m_N}{m_M}\mathcal{O}_{10}$
6	$\frac{1}{m_M}\left(i\Phi_2\overset{\leftrightarrow}{\partial}_\mu\Phi_1\right)Ni\sigma_{\mu\nu}\frac{q^\nu}{m_M}N$	$4i\frac{m_\chi}{m_M}\vec{v}^\perp_{\rm inel}\cdot\left(\frac{\vec{q}}{m_M}\times\vec{S}_N\right)+\frac{m_\chi}{m_N m_M^2}\vert\vec{q}\vert^2\mathbf{1}_\chi\mathbf{1}_N$	$\frac{m_\chi}{m_N m_M^2}\vert\vec{q}\vert^2\mathcal{O}_1-4\frac{m_\chi m_N}{m_M^2}\mathcal{O}_3$
7	$\frac{i}{m_M}\left(i\Phi_2\overset{\leftrightarrow}{\partial}_\mu\Phi_1\right)Ni\sigma_{\mu\nu}\gamma^5\frac{q^\nu}{m_M}N$	$4i\frac{m_\chi}{m_M}\frac{\vec{q}}{m_M}\cdot\vec{S}_N$	$4\frac{m_\chi m_N}{m_M^2}\mathcal{O}_{10}$

TABLE 3. The inelastic relativistic operators for a transition between dark matter particles both of spin 0, $\Phi_1\to\Phi_2$, their matrix element in the nonrelativistic limit after multiplying by a factor of $1/(2m_N)$, and then their decomposition in the basis of allowed scattering matrix elements.

Experimental Input

To analyze the direct detection signal, we take a dark matter density $\rho = 0.3$ GeV/cm^3 [58] and a Maxwell-Boltzmann velocity distribution with parameters $v_0 = 220$ km/s [59] and $v_{\rm esc} = 550$ km/s [60]. For DAMA, since inelastic kinematics favors scattering off of heavier targets, we only consider scattering off of the iodine nuclei in the NaI crystals. We calculated the shift in the best fit points due to Na for operator 2 and found only a 0.07% change in the best fit m_M, and a 0.01% shift in χ^2, so decided not to include Na in the full analysis. We found the modulation rate for scattering off of iodine alone and determined the point in (m_χ, δ, m_M) parameter space which minimized a χ^2 fit against the DAMA/LIBRA data [7]. For our χ^2, we used the first 12 bins of their data, which corresponds to an energy range of 2-8 keV$_{\rm ee}$. Later on, when we plot the 2D parameter space $(\delta, 1/m_M)$, we will show contours for $\Delta\chi^2 = 2.3, 5.99$ representing the $68, 95\%$ C. L. region for two degrees of freedom (*d.o.f.*).

An important parameter in our fits is the quenching factor we adopt for iodine in NaI. The quenching factor Q determines the relationship between the measured energy in electron equivalents, keV$_{\rm ee}$, and the original energy imparted to the nucleus keV$_{\rm nr}$, keV$_{\rm ee} = Q \times$ keV$_{\rm nr}$. Because of this, a good measurement of the quenching factor is necessary to determine the mass splitting and dark matter mass which best fits the DAMA/LIBRA modulation signal as well as determining the constraints from other experiments. For NaI, the value for iodine's quenching factor $Q_I = 0.09$ [61] is widely used, however a more recent paper [62] reports a measurement of $Q_I = 0.04$. We will consider both values for iodine's quenching factor in what follows and denote it by $Q_{\rm NaI}$. A smaller quenching factor shifts the nuclear recoil energies that are relevant to DAMA to higher energies, so even though there is no suppression at xenon targets

for scattering due to kinematics, the energy range could be outside of the acceptance range for LUX and XENON100 (this is more important for LUX as it has a smaller acceptance window). We find that a smaller quenching factor generally requires a larger value of δ to fit the DAMA data which leads to a suppression of scattering at lighter targets like the germanium at CDMS. These considerations mean that an uncertainty in the quenching factor has profound consequences for constraining signals seen in direct detection experiments.

As limits, we first consider the xenon scattering limits in recent analyses by XENON100 [52] and LUX [53]. For XENON100's analysis, there was an exposure of 7.6×10^3 kg $\cdot$ days and the acceptance we used was extracted from the hard discrimination cut of Fig. 1 in [52] used in their maximum gap analysis. This acceptance range is 2 to 43.3 $\mathrm{keV_{nr}}$, though we extended their acceptance window to 50 $\mathrm{keV_{nr}}$ assuming the acceptance didn't change in the last 6.7 $\mathrm{keV_{nr}}$. They observed two events, which we take to be all signal, giving a Poisson 90% C.L. limit of 5.32 events. LUX's analysis had 1.0×10^4 kg $\cdot$ days of exposure and used a 99.6% efficiency after a 50% NR acceptance in an energy range of 10-36 $\mathrm{keV_{nr}}$ (the low energy, 0-10 $\mathrm{keV_{nr}}$, efficiency isn't 99.6% but can be found in the efficiency curve after the single scattering requirements have been accounted for in Fig. 1 of [53]). They observed one event, which we take to be all signal, leading to a Poisson 90% C.L. limit of 3.89 events. As both XENON100 and LUX experiments were primarily searching for elastic dark matter, their energy ranges weren't conducive to a search for inelastic dark matter which favors higher nuclear recoil energies, leading to weakened sensitivities. To be sensitive to these high energy scatters, we also consider an older XENON10 analysis that was focused on inelastic dark matter [51]. This XENON10 analysis had an exposure of 316 kg $\cdot$ days, with an extended energy range of 75-250

keV_{nr} that has a high efficiency $\sim 32\%$, after applying software cuts and nuclear recoil acceptance. They saw no events in their extended range. Since the advantage of this analysis over the more recent xenon experiments is its extended energy range and not its exposure we chose to constrain models if they predict more than 2.3 events (the 90% C.L. limit with no observed events) in this 75-250 keV_{nr} range.

We looked at the constraints from CDMS inelastic dark matter search from their germanium detectors [54] as well. Due to the lighter mass of germanium relative to xenon, we expected its limits would be suppressed relative to xenon limits. This CDMS analysis had 970 kg·days of exposure, and even with perfect acceptance the exclusions for all operators were $\gtrapprox 1000$ times weaker than the limits from the xenon experiments. Thus we decided not to include any more details for germanium detectors.

An important constraint comes from COUPP which employs a CF_3I target [55]. We considered scattering of the dark matter off of the iodine as well as the fluorine, but not the carbon as its form factor isn't available in the Mathematica package. However, due to carbon's light mass, it shouldn't give a significant contribution except for small mass splittings. Our analysis of the COUPP data proceeds similarly to our analysis of the xenon experiments. COUPP had three runs with i) exposures of 70.6 kg·days and an energy threshold of 7.8 keV_{nr}, ii) 88.5 kg·days with an energy threshold of 11 keV_{nr}, and iii) 394 kg·days with an energy threshold of 15.5 keV_{nr}. We considered only single bubble events for which there was a total efficiency of 79.1%, and we used the step-function efficiency model [63] for the iodine nucleation efficiency which rises to 100% above 40 keV_{nr}. Note that we didn't observe a significant shift in the derived limits when using the other parameterized efficiencies [63]. COUPP saw a total of 13 events for all three energy thresholds after time-isolation cuts. Considering these

as signal gives a Poisson 90% C.L. limit of 18.96 events. In all cases, we integrated scatters up to 200 keV_{nr} which covers the range of allowed scatters.

The last experiment we consider is KIMS [56] which has a CsI target. Their analysis has 90% C.L. limits on the dark matter scattering rate in eight bins ranging from 3-11 keV_{ee}. For the purposes of constraining operators we consider a scenario ruled out if the predicted rate in any of these eight bins is larger than the stated limit for that bin. Because KIMS uses CsI there is a different quenching factor for the iodine than the one for NaI crystals. In [64] the quenching factor is measured to be ~ 0.10 over a range of 20 to 120 keV_{nr}. However, similar to NaI, recent results [65] have pointed to a lower value of $Q_I \sim 0.05$ for CsI too. The recent paper only measured CsI doped with sodium, which is not the same as the KIMS detectors which are doped with thallium. However, in light of the new measurement and since the earlier measurement [64] found similar quenching factors for detectors of different doping, a value of $Q_I \sim 0.05$ for the KIMS detectors seems reasonable. Thus, we consider both values in the following analysis and to differentiate it from the iodine quenching factor for NaI, we denote it as Q_{CsI}. As another reminder, we emphasize that we cannot perform this analysis with cesium scattering, so all our constraints from the KIMS experiment are assuming only iodine recoils. Thus, the KIMS limits should get stronger with cesium scattering, but we unfortunately do not know how large of an effect this is.

One other issue we need to consider is the running time of these experiments, since large modulation can lead to order one changes in the scattering rate throughout the year. We use the average scattering rate for XENON100, COUPP, and KIMS since their exposure was accumulated over a year, for LUX we use the maximum rate

since its exposure was obtained during the summer, and for XENON10 we average over its run from October to February.

Reanalysis of Magnetic Inelastic Dark Matter

In this section, we revisit the case of magnetic inelastic dark matter where the transition is mediated by a magnetic dipole transition [43]

$$\mathcal{L} = \frac{\mu_\chi}{2}\bar{\chi}_2\sigma^{\mu\nu}\chi_1 F_{\mu\nu} + h.c. \tag{2.17}$$

Theoretically this scenario is appealing since the tensor operator vanishes for Majorana fermions, naturally leading to an inelastic transition. Furthermore, iodine has a large dipole moment relative to most other heavy nuclear targets, mitigating xenon and tungsten constraints [43]. As mentioned earlier, the form factors used for these scenarios were highly uncertain [43], but we can now reliably calculate them with our modification of the Mathematica code. Note that cesium does have a large dipole moment as well, but since it isn't implemented in the Mathematica notebook, we unfortunately have to neglect its scattering contribution.

To calculate the form factor for the dipole transition, we use the following coefficients for the fermion operators 9 and 10 involving protons and neutrons

$$\begin{aligned}\mathcal{L}_{\text{MIDM}} = \frac{1}{q^2}\left[\bar{\chi}_2 i\sigma^{\mu\nu}\frac{q_\nu}{m_M}\chi_1\ \bar{p}\gamma_\mu p\right] &+ 0.9\frac{m_M}{m_N q^2}\left[\bar{\chi}_2 i\sigma^{\mu\nu}\frac{q_\nu}{m_M}\chi_1\ \bar{p}i\sigma_{\mu\alpha}\frac{q^\alpha}{m_M}p\right] \\ &- 0.96\frac{m_M}{m_N q^2}\left[\bar{\chi}_2 i\sigma^{\mu\nu}\frac{q_\nu}{m_M}\chi_1\ \bar{n}i\sigma_{\mu\alpha}\frac{q^\alpha}{m_M}n\right]\end{aligned} \tag{2.18}$$

$Q_{\rm NaI}$	m_χ(GeV)	δ(keV)	m_M(GeV)	$\chi^2/d.o.f.$	$r^{90\%}_{\rm XENON10}$	$r^{90\%}_{\rm XENON100}$	$r^{90\%}_{\rm LUX}$	$r^{90\%}_{\rm COUPP}$	$r^{90\%}_{\rm KIMS,0.10}$	$r^{90\%}_{\rm KIMS,0.05}$
Magnetic Inelastic Dark Matter										
0.09	58.0	111.7	3209	0.97	0.0002	17.500	67.5	1.39	1.17	0.08
0.04	122.7	179.3	1096	0.82	0.2943	0.284	0.0	1.32	0.97	0.93

TABLE 4. This table presents the best fit parameters to the DAMA/LIBRA data for the magnetic dipole transition operator and its $\chi^2/d.o.f.$ value. For these operators, the couplings are defined in Eq. 2.18. The final five columns give normalized limits, with the ratio of predicted to 90% C.L. allowed counts for XENON10, XENON100, LUX, and COUPP and the largest ratio of the KIMS bins counts/kg·days/keV over the 90% C.L. limit (this limit is presented for two different iodine quenching factors for KIMS, $Q_{\rm CsI}$). There is a fit for two values of the iodine quenching factor for NaI $Q_{\rm NaI} = 0.09, 0.04$. Due to data taking conditions, the values for the XENON100, COUPP, and KIMS columns use the average yearly rate, the rate for LUX was the maximum, and the rate for XENON10 was averaged from October to February.

The relative coefficients are set by the proton and neutron magnetic moments being 2.8 and -1.91 nuclear magnetons, respectively. Given the overall normalization, the relationship between our m_M and the dark matter dipole moment is $1/m_M = e\mu_\chi$.

The best fit points in this parameter space are shown in Table 4 for the two choices of quenching factor, $Q_{\rm NaI} = 0.09$, 0.04. The $\chi^2/d.o.f.$ for our fit to DAMA is shown, with a $d.o.f. = 9$, showing a very nice goodness of fit. The final six columns show the normalized limits, r, from xenon and iodine experiments so that r values above 1 are constrained at 90% C.L. For XENON10, XENON100, LUX, and COUPP experiments, r is the ratio of predicted events over the number of events allowed at 90% C.L. (2.3, 5.32, 3.89, and 18.96 respectively). For KIMS, in each bin from 3-11 $\rm keV_{ee}$ we take the predicted bin rate divided by the 90% C.L. limit on the rate in that bin, with r being the largest of these bin ratios. We list KIMS constraints where we assume two values of the quenching factor $Q_{\rm CsI} = 0.10$ and 0.05 for CsI. Notice that for $Q_{\rm NaI} = 0.04$, the scenario is narrowly excluded by COUPP while being unconstrained by the other experiments.

Xenon Constraints

The strength of the LUX or XENON100 limit depends strongly on the value of $Q_{\rm NaI}$ we choose. For the standard value $Q_{\rm NaI} = 0.09$, the $2-6$ $\rm keV_{ee}$ energy range of DAMA's modulation spectra is $\sim 22-67$ $\rm keV_{nr}$. With the lower value of $Q_{\rm NaI} = 0.04$ this changes to a much higher range of $50-150$ $\rm keV_{nr}$. For inelastic dark matter, the modulated and unmodulated spectra span roughly the same energy bins and since xenon's mass is similar to iodine, the scattering off xenon will be roughly in the same range of nuclear recoil energies. This explains why the LUX constraints are noticeably weaker for $Q_{\rm NaI} = 0.04$, since its acceptance goes to zero above ~ 36 $\rm keV_{nr}$

while XENON100's goes up to 50 keV_{nr}. This acceptance helps to make XENON100 competitive despite its smaller exposure.

To show this effect, we look at the best fit spectra for magnetic inelastic dark matter with different Q_{NaI} values. We saw that XENON100 and LUX were a strong constraint for the larger value of the quenching factor, but the constraints for $Q_{\text{NaI}} = 0.04$ were much weaker. This is directly related to the location of the scattering spectrum relative to the experimental acceptance windows as shown in Fig. 3. For $Q_{\text{NaI}} = 0.09$, the peak of the spectrum is well covered by both experiments, leading to the stringent constraints. However, for $Q_{\text{NaI}} = 0.04$, the peak scattering is missed by both experiments, with LUX having no sensitivity. Given these high energy events, we also checked the constraints from XENON10's inelastic dark matter analysis [51] which extended to much higher energies. In Fig. 3 and Table 4, one can see that this XENON10 constraint is slightly stronger for the smaller iodine quenching factor, but is still not able to constrain this scenario due to its low exposure. On the other hand, in existing XENON100 or LUX data there are about ~ 100 events at high energy, so we encourage an extension of their analysis to energies above 50 keV_{nr}. If the background in this region can be kept under control, they would have a high sensitivity to this scenario.

Iodine Constraints

As expected, the constraints from other iodine detectors are very stringent for most inelastic dark matter scenarios since this is a direct comparison of the same target. For COUPP constraints, changing Q_{NaI} hardly affects the constraints. The energy thresholds of the COUPP runs are not too high to lose many low energy events and the acceptance at high energy means that COUPP is sensitive to essentially all

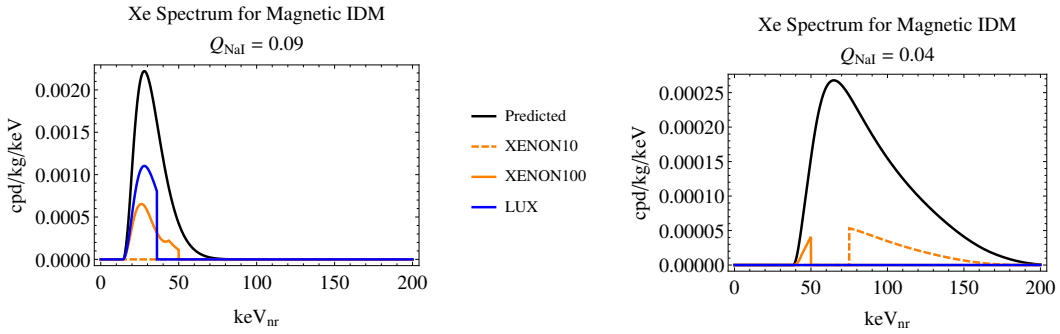

FIGURE 3. These figures shows the xenon scattering spectrum for the best fit to DAMA's signal for magnetic inelastic dark matter for two choices of $Q_{\rm NaI}$. The black curve is the expected spectrum while the orange (blue, orange-dashed) curve is the accepted spectrum for XENON100 (LUX, XENON10). Note that for $Q_{\rm NaI} = 0.09$ the peak is visible to both XENON100 and LUX, but for $Q_{\rm NaI} = 0.04$ both these experiments' acceptances are too low at high energy to see a significant number of events.

of the iodine scattering relevant for DAMA. This explains why COUPP is the best constraint on DAMA both in terms of sensitivity and robustness from quenching factor uncertainties.

For KIMS, if the iodine quenching values used by the DAMA and KIMS experiments, $Q_{\rm NaI} = 0.09, Q_{\rm CsI} = 0.10$ are correct, the best fit point for magnetic inelastic dark matter is ruled out. These constraints show a strong dependence on the quenching factor values chosen. As the recent work of [62] and [65] shows, the correct values are not pinned down yet and could be significantly smaller. This is especially relevant to KIMS constraints, since the scattering spectrum can be substantially shifted in energy, allowing much weaker constraints for some choices of the quenching factors. As an illustration, we show in the four plots of Fig. 4 how the spectra at KIMS shifts as we change the two quenching factors. In the upper left plot, we see that for the quenching factors $Q_{\rm NaI} = 0.09, Q_{\rm CsI} = 0.10$, the best fit point is constrained in the lowest KIMS bin. However, in the upper right plot, changing to $Q_{\rm CsI} = 0.05$, we see that the spectrum shifts to energy bins below their threshold, giving no constraint.

In general, such a combination of quenching factors leads to particular weak limits from KIMS due to the scattering moving below threshold. In the bottom left, the benchmark point with $Q_{\rm NaI} = 0.04, Q_{\rm CsI} = 0.10$, leads to a mild constraint in the 6 keV_{ee} bin. In the bottom right, changing the CsI quenching factor to 0.05, the spectrum shifts to lower values again leading to a rate that is almost constrained in the first bin with a smaller normalized limit, r. Given the uncertainties, we consider both CsI quenching factors in presenting KIMS limits. However, if the same physics leads to the quenching factors of NaI and CsI to be of similar size, we find that KIMS becomes a more robust constraint.

Up to these quenching factor issues, iodine targets still provide the most model independent constraints on scenarios where iodine scattering explains the DAMA signal. For these cases, the only way to suppress scattering is to have higher modulation amplitude. Since COUPP and KIMS both ran over a year, this can lead to a modest drop in sensitivity which explains why the higher δ point has weaker constraints.

Combined Limit Plots for Magnetic Inelastic Dark Matter

Although the best fit points for magnetic inelastic dark matter are ruled out conclusively by COUPP, there can be viable regions of parameter space which maintain a decent fit to DAMA. To search for these we fix the best fit dark matter mass and then explored the remaining two dimensional parameter space in (δ, m_M). For DAMA, the $68, 95\%$ C.L. parameter estimation regions were computed relative to the best fit χ^2. As can be seen in the left plot of Fig. 5, if $Q_{\rm NaI} = 0.09$, the constraints from LUX and XENON100 are strong and rule out all of the DAMA parameter space. However, for the case of $Q_{\rm NaI} = 0.04$, the right plot of Fig. 5

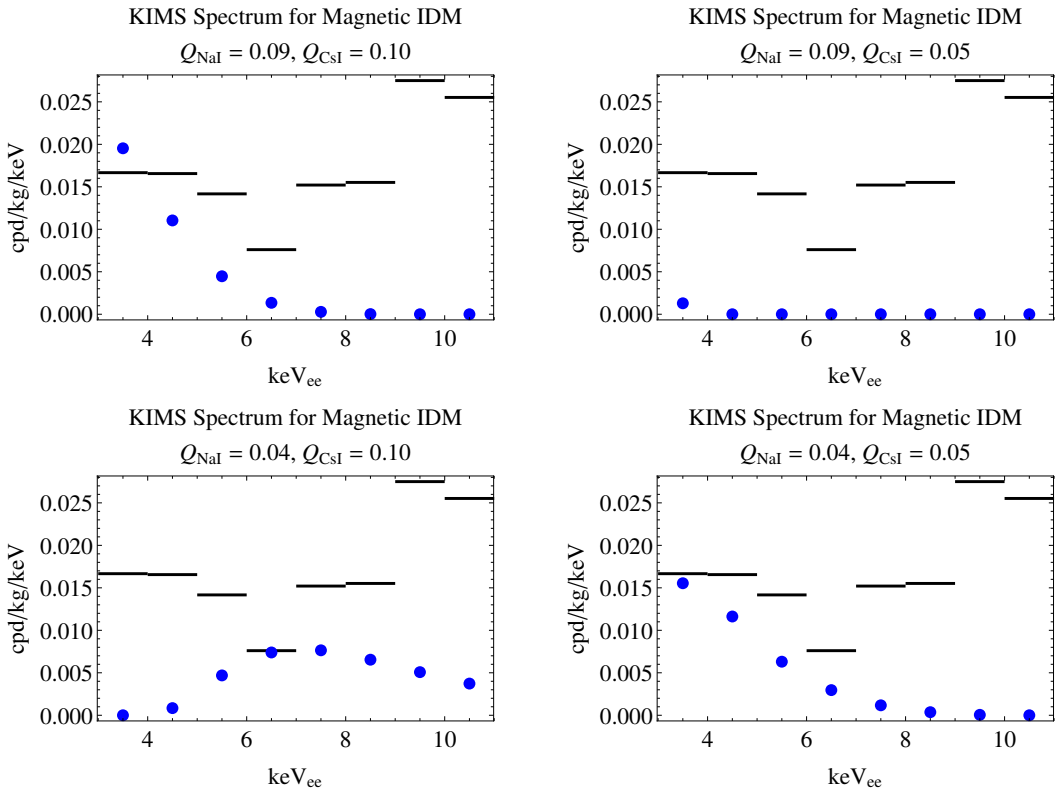

FIGURE 4. This figure shows the KIMS energy spectrum for scattering events for magnetic inelastic dark matter at different $Q_{\rm NaI}$'s and $Q_{\rm CsI}$'s. The blue points are the best fit points predicted rates and the black lines are the 90% limits in each KIMS bin [56]. Notice that the peak can shift from lower to higher energies as the quenching factors vary causing significant changes to the limit.

shows that the constraints from all experiments weaken as one moves to higher values of the mass splitting, leading to a sliver of the 68% C.L. DAMA region which is not constrained and a significant region allowed at 95% C.L. That XENON10 and the iodine experiments slowly fall off with increasing mass splitting shows how these experiments are mostly being weakened by increasing modulation and not a change in the energy spectrum.

In Fig. 6, we show the modulation spectra for the best fit point and an unconstrained point with the DAMA data points for comparison. We see that the increase in mass splitting leads to a degradation in the χ^2 but still has a good fit

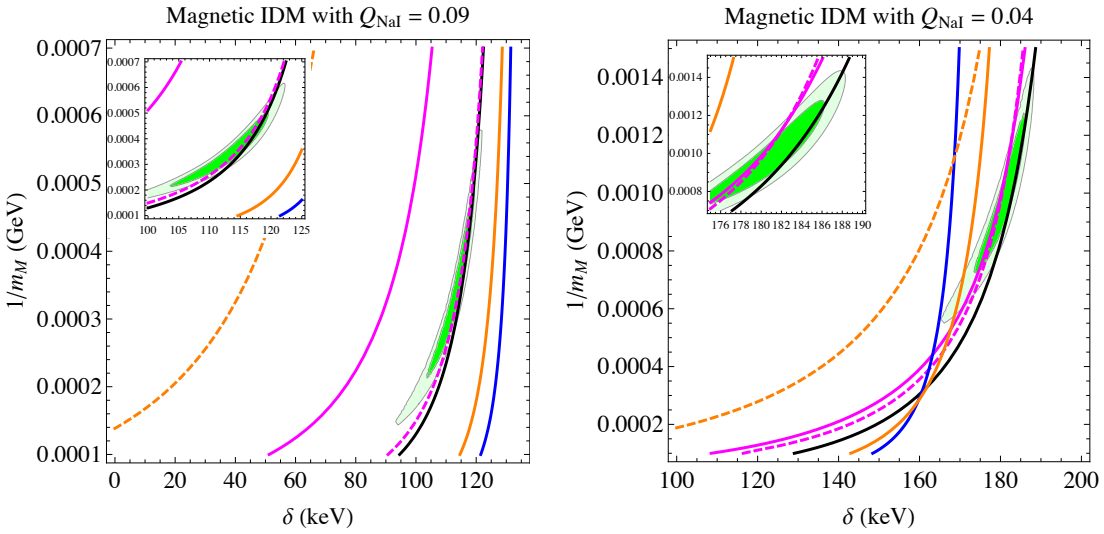

FIGURE 5. This figure shows the combined limits plots for magnetic inelastic dark matter. The DM masses used are those listed with the corresponding quenching factor in Table 4. Constraints from LUX (blue), XENON100 (orange), XENON10 (orange dashed), KIMS ($Q_{\rm CsI} = 0.05$ magenta solid, $Q_{\rm CsI} = 0.10$ magenta dashed) and COUPP (black) are also shown, with the 90% C.L. limits listed in section 2.3.

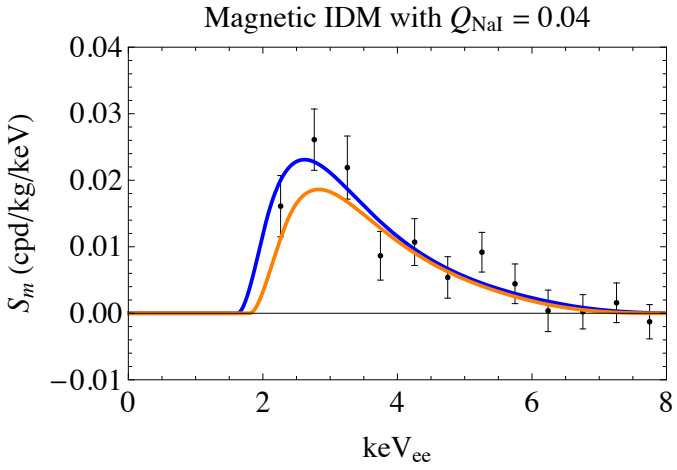

FIGURE 6. This shows the magnetic inelastic dark matter modulation amplitudes with the DAMA data points for comparison. The plot assumes a iodine quenching factor $Q_{\rm NaI} = 0.04$ and has both the best-fit modulation amplitude in blue and a sample unconstrained fit in orange. For nine $d.o.f.$, the parameter values for the best fit are $(m_\chi, \delta, m_M) = (122.7\ \text{GeV}, 179.3\ \text{keV}, 1096\ \text{GeV})$ with $\chi^2/d.o.f. = 0.82$ and for the unconstrained point are $(m_\chi, \delta, m_M) = (122.7\ \text{GeV}, 184.5\ \text{keV}, 952\ \text{GeV})$ with $\chi^2/d.o.f. = 1.17$.

to the DAMA spectra. Note that the values of $1/m_M$ required are quite reasonable since the magnetic moment of a particle should be of order a dark matter "magneton" $= e/(2m_\chi)$, so that $1/m_M \sim e^2/(2m_\chi) = 5 \times 10^{-4}(\frac{100 \text{ GeV}}{m_\chi})$. The required magnetic moment seems to be similar to those seen in the nucleon sector and thus it seems plausible that this part of parameter space could appear generically in a complete model of magnetic inelastic dark matter.

General Model Independent Analysis

Now, we consider a more general model independent search for consistent scenarios that explain the DAMA annual modulation signal. We performed a survey of the relativistic operators listed in Tables 1-3 by analyzing the scattering when only one operator is turned on at a time. Depending on the operator, we need to multiply by a dimensionful coupling λ to describe the effective operator in the Lagrangian. For the fermion operators, we took this coupling to be $\lambda = 1/m_M^2$, so that m_M characterizes the scale of the effective operator. For the bosonic cases, we instead take $\lambda = 1/m_M$. Thus the parameters we varied were the dark matter mass m_χ, the dimensional coupling parameter m_M, and the mass splitting δ.

To narrow our survey and to specifically avoid the stringent constraints of xenon target experiments, we only considered operators whose transition probabilities for iodine were significantly ($\geq$ 10 times) enhanced over xenon. These operators were identified by examining the ratio of iodine's transition probability to xenon's at the minimum velocity for iodine (see Eq. 2.7), as it is higher than the minimum velocity for xenon scattering. This ratio was plotted, for a specific value of m_χ on the (δ, E_R) plane with E_R the nuclear recoil energy (the parameter m_M cancels in the ratio). The operators' coupling to nucleons was varied between pure proton, pure neutron, equal

Op. #	$Q_{\rm NaI}$	m_χ(GeV)	δ(keV)	m_M(GeV)	$\chi^2/d.o.f.$	$r^{90\%}_{\rm XENON100}$	$r^{90\%}_{\rm LUX}$	$r^{90\%}_{\rm COUPP}$	$r^{90\%}_{\rm KIMS,0.10}$	$r^{90\%}_{\rm KIMS,0.05}$
Spin 1/2 $\rightarrow$ 1/2 Transition										
2	0.09	44.2	59.0	15.9	1.08	0.049	0.130	3.28	2.27	0.21
	0.04	84.6	103.2	17.4	1.03	0.006	0.014	4.23	2.50	2.16
4	0.09	40.8	57.0	0.5	1.15	0.030	0.082	2.77	2.08	0.06
	0.04	61.8	0.0	1.0	1.01	0.035	0.072	10.30	5.17	4.30
7	0.09	55.3	108.3	1.6	0.97	0.017	0.053	1.41	1.09	0.11
	0.04	111.8	163.2	1.5	0.97	0.001	0.000	1.81	1.22	1.12
8	0.09	44.2	59.0	7.8	1.08	0.049	0.130	3.28	2.27	0.21
	0.04	84.6	103.2	8.3	1.03	0.006	0.014	4.23	2.50	2.16
9	0.09	47.4	69.0	4.6	1.01	40.420	117.900	3.00	2.19	0.21
	0.04	95.1	135.1	4.0	0.99	1.791	2.847	2.79	1.83	1.59

TABLE 5. This table presents the best fit parameters to the DAMA/LIBRA data for each fermionic operator for which iodine showed an enhancement over xenon, considering proton coupling *only*, and their $\chi^2/d.o.f.$ value. For these fermion operators, the coupling is $\lambda = 1/m_M^2$. The final five columns give normalized limits, with the ratio of predicted to 90% C.L. allowed counts for XENON100, LUX, and COUPP and the largest ratio of the KIMS bins counts/kg·days/keV over the 90% C.L. limit (this limit is presented for two different iodine quenching factors for KIMS, $Q_{\rm CsI}$). Each operator has a fit for two values of the iodine quenching factor for NaI $Q_{\rm NaI} = 0.09$, 0.04. Due to data taking conditions, the values for the XENON100, COUPP, and KIMS columns uses the average yearly rate, and the rate for LUX was the maximum.

Op. #	$Q_{\rm NaI}$	m_χ(GeV)	δ(keV)	m_M(GeV)	$\chi^2/d.o.f.$	$r^{90\%}_{\rm XENON100}$	$r^{90\%}_{\rm LUX}$	$r^{90\%}_{\rm COUPP}$	$r^{90\%}_{\rm KIMS,0.10}$	$r^{90\%}_{\rm KIMS,0.05}$
Spin $1/2 \to 1/2$ Transition										
10	0.09	40.9	53.2	2.5	1.06	0.111	0.284	3.12	2.21	0.09
	0.04	62.4	0.0	3.7	1.00	0.156	0.282	12.67	5.26	4.34
11	0.09	50.8	96.6	5.8	1.11	0.042	0.119	1.72	1.29	0.10
	0.04	85.5	106.4	7.7	1.03	0.032	0.056	4.26	2.44	2.10
13	0.09	56.1	110.9	19.6	0.96	13.640	55.640	1.32	1.08	0.08
	0.04	112.6	170.7	15.6	0.94	0.751	0.015	1.42	0.97	0.92
14	0.09	50.8	96.6	5.8	1.11	0.042	0.119	1.72	1.29	0.10
	0.04	85.5	106.4	7.7	1.03	0.032	0.056	4.26	2.44	2.10
15	0.09	54.3	106.0	49.6	1.02	0.021	0.069	1.49	1.15	0.10
	0.04	102.7	146.8	54.3	1.00	0.005	0.006	2.47	1.60	1.44
19	0.09	52.6	97.5	0.6	1.02	0.045	0.139	1.66	1.23	0.09
	0.04	99.9	137.7	0.7	1.01	0.012	0.015	2.18	1.36	1.20
20	0.09	40.8	57.0	2.5	1.15	0.030	0.082	2.77	2.08	0.06
	0.04	61.8	0.0	3.9	1.01	0.035	0.072	10.30	5.17	4.30

coupling to proton and neutron, and equal but opposite couplings. We found that only pure coupling to protons significantly favored iodine over xenon and further that all iodine-enhanced operators had some contribution from the nucleon spin $\vec{\mathcal{O}}_3^N$, see Eq. 2.12. Since iodine's nucleus has an unpaired proton while xenon has an unpaired neutron, this explains why the sensitivity is enhanced if we only couple to the proton [66]. As a check that this method for selecting operators finds all relevant ones, we also performed a full analysis for several other operators and nucleon couplings and found the results matched our predictions from this selection process. Note that our inability to treat cesium in KIMS is particularly important for coupling to proton spin, since cesium also has an unpaired proton. On the other hand, tungsten isotopes only have unpaired neutrons, so we expect that their rates would be suppressed much like xenon targets.

The best fit points in this parameter space is shown in Tables 5 and 6 for the two choices of quenching factor of $Q_{\rm NaI} = 0.09$, 0.04. The $\chi^2/d.o.f.$ for our fit to DAMA is shown, with a $d.o.f. = 9$, showing a reasonable goodness of fit for all operators. The final five columns show the normalized limits, r, from xenon and iodine experiments so that r values above 1 are constrained at 90% C.L. For XENON100, LUX, and COUPP experiments, r is the ratio of predicted events over the number of events allowed at 90% C.L. (5.32, 3.89, and 18.96 respectively). For KIMS, in each bin from 3-11 keV_{ee} we take the predicted bin rate divided by the 90% C.L. limit on the rate in that bin, with r being the largest of these bin ratios. We list KIMS constraints where we assume two values of the quenching factor $Q_{\rm CsI} = 0.10$ and 0.05 for CsI. Notice that there are a few operators which are narrowly excluded by COUPP while being unconstrained by the other experiments.

Even though we've discussed how XENON10 is sensitive to much higher energy scatters than XENON100 or LUX, we find that it generically sets weaker constraints for this model independent analysis due to its lower exposure. In a few cases, the limits of XENON10 were similar or just a bit larger than XENON100, for example fermion operators 7, 15, and 19, spin 0 to 1 operators 6, and spin 0 to 0 operator 4, but they were not large enough to be constraining. Because these constraints were not strong enough to rule out any best fit points, we chose not to include the XENON10 limits in our tables or figures for this model independent survey.

Combined Limit Plots for Relativistic Operators

Although the best fit points are ruled out conclusively by COUPP, we still find viable regions of parameter space which maintain a decent fit to DAMA, similar to the case of magnetic inelastic dark matter. For some of the operators, we found that the DAMA regions could stretch far into the high δ region of parameter space. The resulting increase in modulation can lead to consistency with the COUPP and KIMS constraints. The fermion operators which have such an allowed region are operator 2 for $Q_{\rm NaI} = 0.09$, operator 7 for both quenching factors, operator 9 for $Q_{\rm NaI} = 0.04$, 11 for $Q_{\rm NaI} = 0.09$, 13 for $Q_{\rm NaI} = 0.04$, 15 with both quenching factors, and 19 with both quenching factors. Also the scalar to scalar operator 4 has a consistent region for both quenching factors. For these operators, we have plotted the allowed regions in Fig. 7 and 8. One again can see that the key to avoiding constraints is moving to higher δ. Thus, the allowed spectra at DAMA will again generically be at slightly higher energy with a slight reduction in the overall amplitude, similar to what was seen in Fig. 6. In this list of allowed operators, we ignored degeneracies in scattering form factors where we have the families i) fermion 2, fermion 8, scalar 2, and scalar 5,

Op. #	$Q_{\rm NaI}$	m_χ(GeV)	δ(keV)	m_M(GeV)	$\chi^2/d.o.f.$	$r^{90\%}_{\rm XENON100}$	$r^{90\%}_{\rm LUX}$	$r^{90\%}_{\rm COUPP}$	$r^{90\%}_{\rm KIMS,0.10}$	$r^{90\%}_{\rm KIMS,0.05}$
Spin $0 \to 1$ Transition										
4	0.09	40.8	57.0	0.5	1.15	0.030	0.082	2.77	2.08	0.06
	0.04	61.8	0.0	1.0	1.01	0.035	0.072	10.30	5.17	4.30
5	0.09	40.8	57.0	0.5	1.15	0.030	0.082	2.77	2.08	0.06
	0.04	61.8	0.0	1.0	1.01	0.035	0.072	10.30	5.17	4.30
6	0.09	54.3	106.0	22.6	1.02	0.021	0.069	1.49	1.15	0.10
	0.04	102.7	146.8	14.3	1.00	0.005	0.006	2.47	1.60	1.44
7	0.09	50.8	96.6	1.4	1.11	0.042	0.119	1.72	1.29	0.10
	0.04	85.5	106.4	1.6	1.03	0.032	0.056	4.26	2.44	2.10
Spin $0 \to 0$ Transition										
2	0.09	44.2	58.2	1.0	1.08	0.049	0.127	3.32	2.29	0.21
	0.04	84.6	103.3	1.1	1.03	0.005	0.013	4.21	2.49	2.15
4	0.09	56.6	108.7	1.0	0.99	0.011	0.041	1.48	1.16	0.10
	0.04	115.6	166.7	1.3	0.96	0.001	0.000	1.76	1.21	1.12
5	0.09	44.2	58.2	1.0	1.08	0.049	0.127	3.32	2.29	0.21
	0.04	84.6	103.3	1.1	1.03	0.005	0.013	4.21	2.49	2.15
7	0.09	44.2	58.2	3.7	1.08	0.049	0.127	3.32	2.29	0.21
	0.04	84.6	103.3	4.5	1.03	0.005	0.013	4.21	2.49	2.15

TABLE 6. This table presents the best fit parameters to the DAMA/LIBRA data for each bosonic operator for which iodine showed an enhancement over xenon, considering proton coupling *only*, and their $\chi^2/d.o.f.$ value. The coupling is $\lambda = 1/m_M$. The final five columns give normalized limits, with the ratio of predicted to 90% C.L. allowed counts for XENON100, LUX, and COUPP and the largest ratio of the KIMS bins counts/kg·days/keV over the 90% C.L. limit. Each operator has a fit for two values of the iodine quenching factor for NaI $Q_{\rm NaI} = 0.09$, 0.04. Due to data taking conditions, the values for the XENON100, COUPP, and KIMS columns uses the average yearly rate, and the rate for LUX was the maximum.

ii) fermion 11, fermion 14, and scalar to vector 7, iii) fermion 15 and scalar to vector 6. These families share allowed parameter space, although different values for m_M are required to get the same rate. Interestingly, some operators whose best fit values are only narrowly ruled out remain ruled out in these two dimensional scans. For instance, fermion operators 4, 10, 20 and scalar to scalar operator 7 have reasonable constraints for $Q_{\rm NaI} = 0.09$. In these cases, the form factors do not allow good DAMA fits to persist to higher δ thus making it impossible to avoid the constraints.

Conclusions

We have shown that a nonrelativistic effective theory for the inelastic scattering of dark matter off a nucleus is a straightforward extension of elastic scattering. The modifications revolve around the Galilean-invariant, incoming dark matter velocity. Due to the inelastic kinematics, the components of the incident velocity that are perpendicular to the momentum transfer $\vec{q}$ have a new piece that depends on the mass splitting δ

$$\vec{v}^{\perp}_{\rm inel} \equiv \vec{v} + \frac{\vec{q}}{2\mu_N} + \frac{\delta}{|\vec{q}|^2}\vec{q}. \tag{2.19}$$

This variable change motivates a new basis of scattering matrix elements written in terms of $\vec{v}^{\perp}_{\rm inel}$. As an application, we have shown how inelastic transitions of a fermion to fermion, scalar to scalar, and scalar to vector can be written in terms of this basis. Finally, since the nuclear matrix elements for most cases only depend linearly on this velocity, we were able to modify the Mathematica code [32] to generate the form factors for inelastic scattering processes. Thus, our work extends the framework of [11]

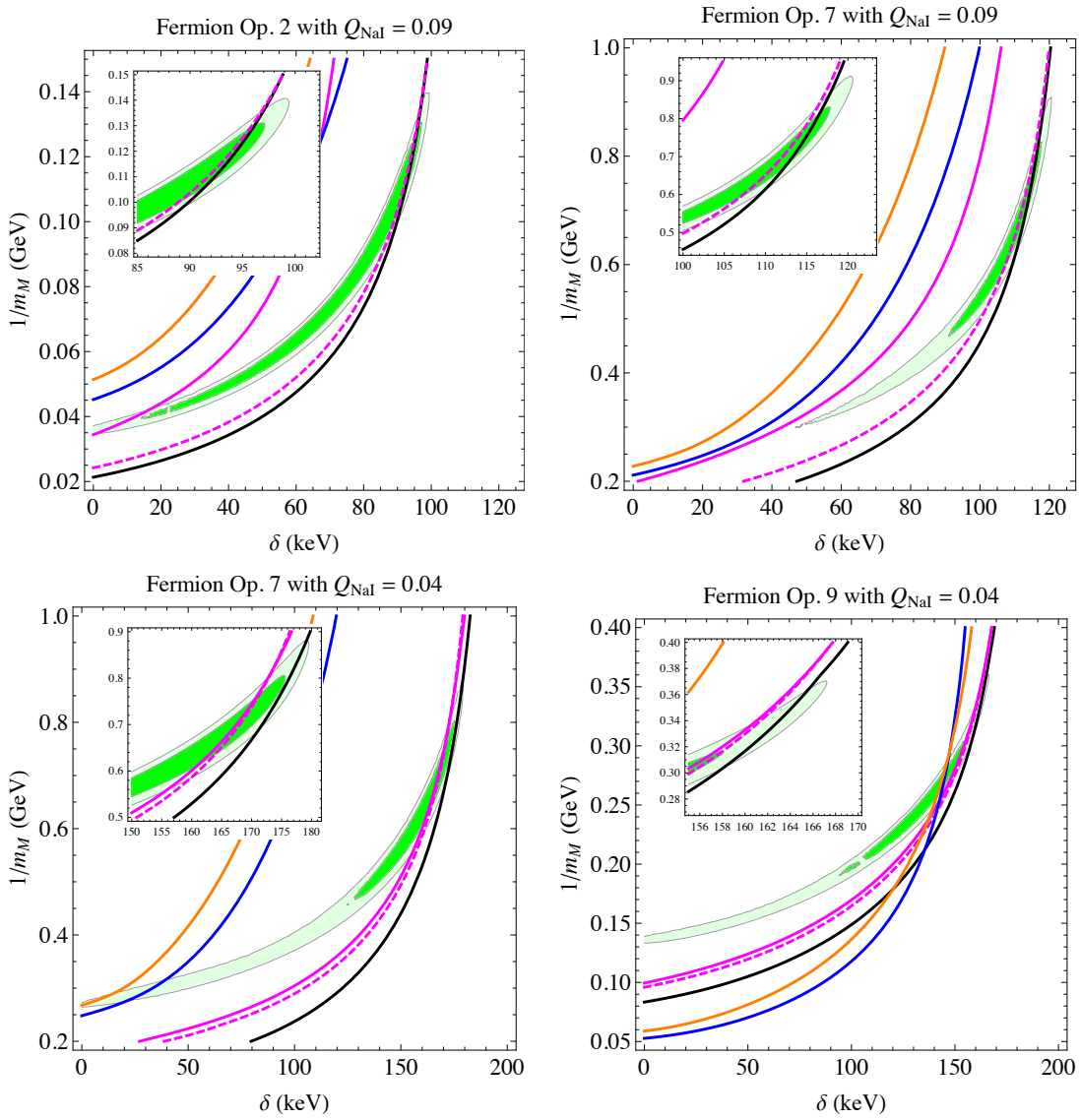

FIGURE 7. This figure shows the combined limits plots for operators which have an unconstrained region that fits the DAMA signal. The DM masses used are those listed with the corresponding operator in Table 5. Constraints from LUX (blue), XENON100 (orange), KIMS ($Q_{\rm CsI}$ = 0.05 magenta solid, $Q_{\rm CsI}$ = 0.10 magenta dashed) and COUPP (black) are also shown, with the 90% C.L. limits listed in section 2.3.

so that inelastic dark matter transitions can now be treated in a model independent fashion.

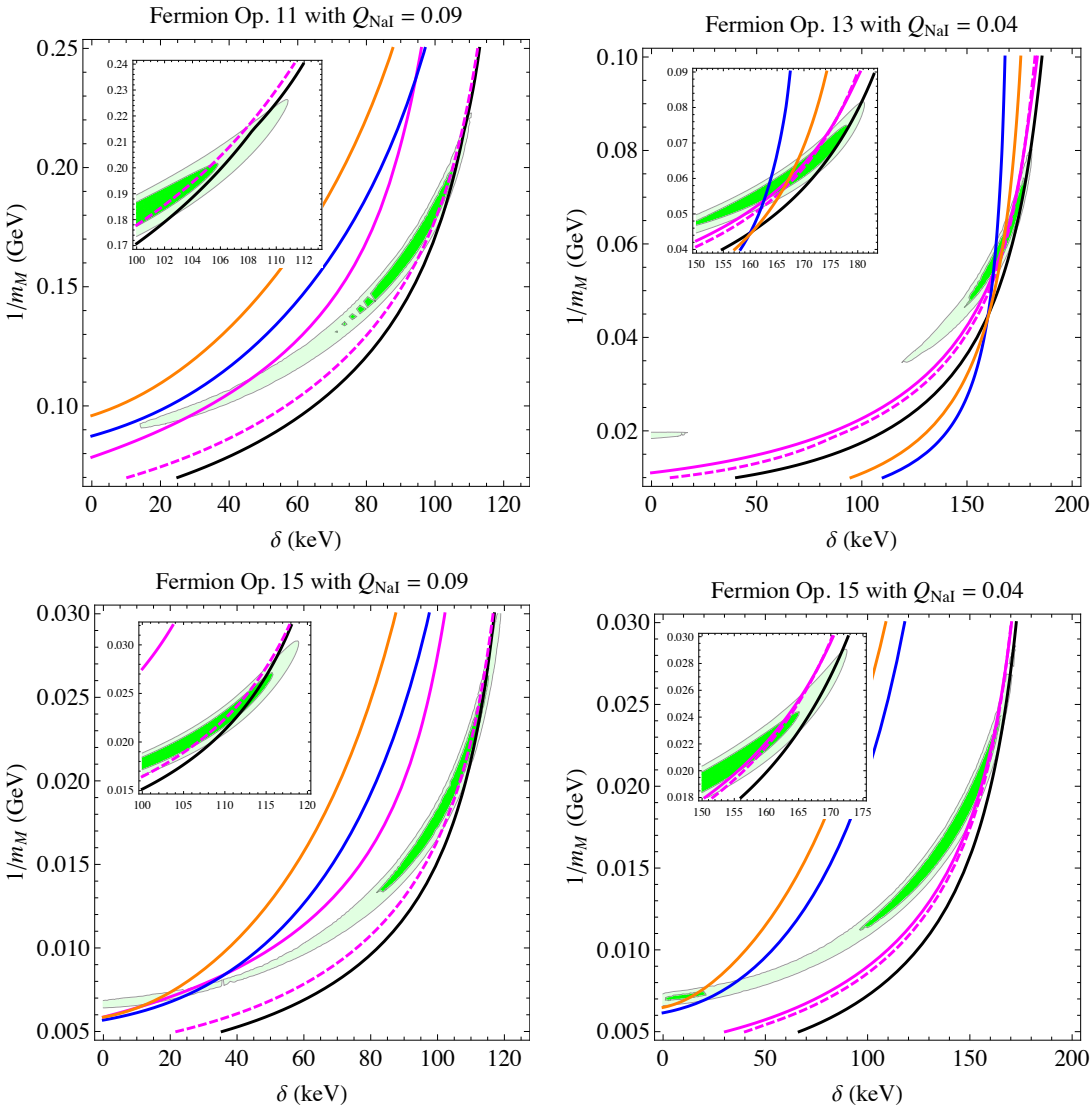

FIGURE 8. This figure shows the combined limits plots for more operators which have an unconstrained region that fits the DAMA signal. The DM masses used are those listed with the corresponding operator in Tables 5, 6. Constraints from LUX (blue), XENON100 (orange), KIMS ($Q_{\rm CsI} = 0.05$ magenta solid, $Q_{\rm CsI} = 0.10$ magenta dashed) and COUPP (black) are also shown, with the 90% C.L. limits listed in section 2.3.

Armed with our effective theory, we then created several fits to the DAMA/LIBRA annual modulation. We considered both the scenario of magnetic inelastic dark matter as well as a model independent survey looking at individual

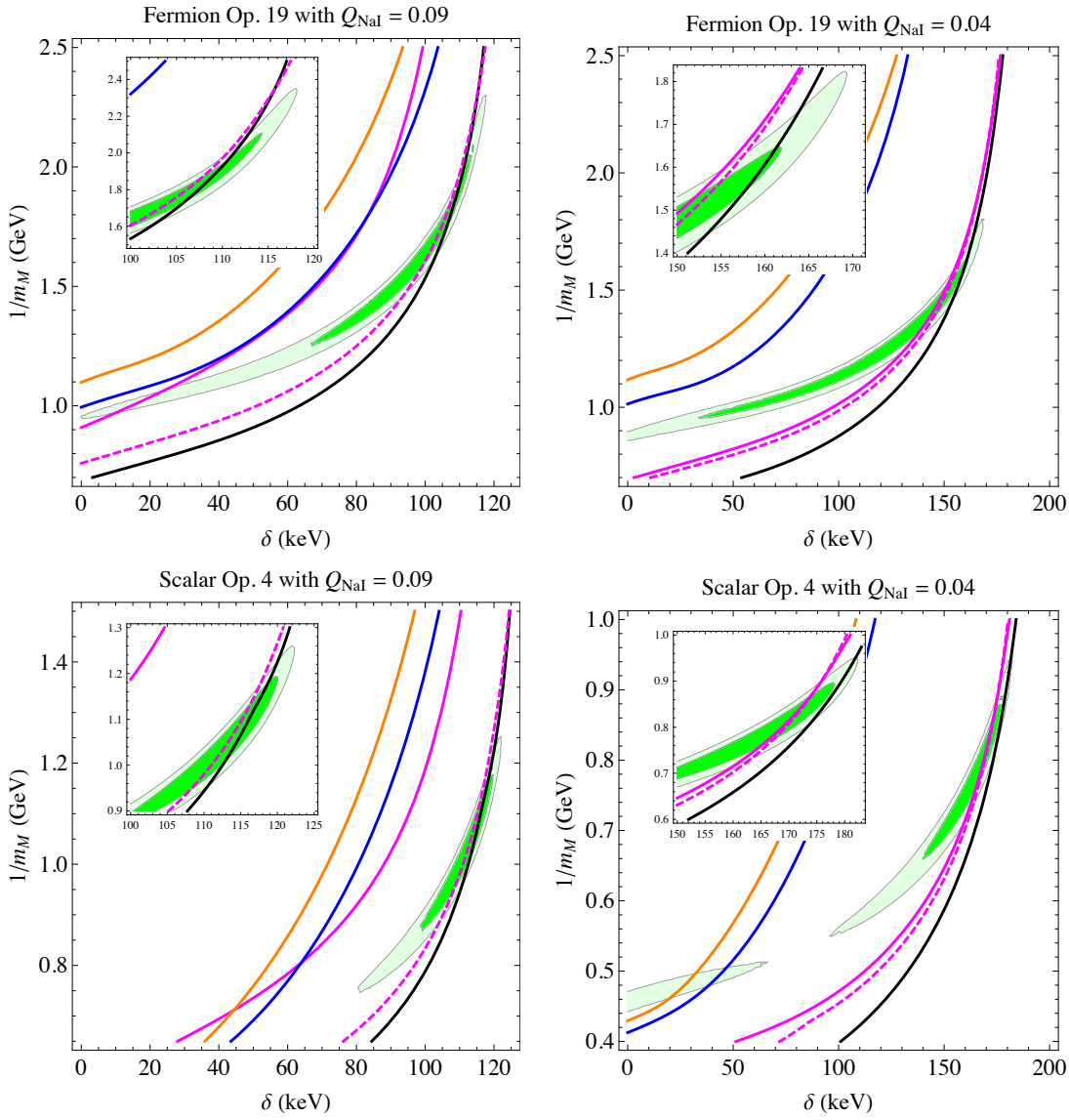

FIGURE 9. This figure shows the combined limits plots for the remaining operators which have an unconstrained region that fits the DAMA signal. The DM masses used are those listed with the corresponding operator in Tables 5, 6. Constraints from LUX (blue), XENON100 (orange), KIMS ($Q_{\rm CsI} = 0.05$ magenta solid, $Q_{\rm CsI} = 0.10$ magenta dashed) and COUPP (black) are also shown, with the 90% C.L. limits listed in section 2.3.

relativistic operators. Due to the strong constraints from XENON100 and LUX, in the model independent scan, we considered choices for the nucleon couplings that would enhance iodine scattering over xenon. This led us to consider operators involving

only couplings to protons that are sensitive to the proton spin. CDMS constraints by comparison are significantly weaker due to germanium's lighter mass and even smaller proton spin. However, we showed that there are significant constraints from the iodine experiments KIMS and COUPP, which provide a mostly model-independent constraint. These limits are thus harder to avoid; we find that they can only be weakened by enhanced modulation or by uncertainties in the iodine quenching factors, which affect the KIMS limits.

For the case of magnetic inelastic dark matter and for some of the relativistic operators involving only proton couplings, we found that scenarios could be consistent with the DAMA fit and existing constraints. However, we would like to stress that we are not able to definitively claim a consistent explanation of the DAMA signal. First of all, due to lack of implementation, we could not treat scattering off of cesium or tungsten, which are relevant for KIMS and CRESST. Cs in particular has an unpaired proton and should lead to stronger constraints from KIMS. Hopefully in a future update of the notebook [32], these elements could be included. Second, we only tested the relativistic *operators* using our effective theory. No models explaining these interactions were considered and thus in a complete model may run into difficulties when confronted with other dark matter constraints. However, it would be interesting to look at complete models realizing these scenarios, which we leave to future work. In particular, the magnetic inelastic dark matter scenario should be straightforward to build in a model, since the required coupling structure is through the standard electromagnetic couplings (for specific realizations see refs. [67, 68]).

In the near future, these models should be definitively tested from direct detection experiments alone. To do so, one high priority is resolving the current uncertainty in iodine quenching factors so as to both pin down the DAMA parameter

space and firm up the constraints from KIMS. Existing data at XENON100 and LUX at energies above 50 $\mathrm{keV_{nr}}$ should also be reanalyzed which will enhance sensitivities to scenarios when the iodine quenching factor is low. Finally, iodine target experiments are the most robust tool to rule out or discover these scenarios. In particular, COUPP's next analysis should give us a definitive answer whether iodine scattering scenarios are a consistent explanation of DAMA's annual modulation signal.

CHAPTER III

CORRELATED SIGNALS AT THE ENERGY AND INTENSITY FRONTIERS FROM NONABELIAN KINETIC MIXING

This chapter is based on previously published and unpublished, co-authored material[1].

In the previous chapter I discussed an analysis of dark matter interactions with nuclear matter. The analysis presented was model independent in that it focused on a complete basis of interaction operators for low energy scattering. This naturally suggests the question: how can these interactions be generated? There are many ways to generate the interactions discussed in the previous chapter, but many such methods are highly unnatural in the sense that parameters of the Lagrangian have to be tuned to produce careful cancellations in the non-relativistic limit. In addition to the precise form of the interaction, the required weakness of the dark matter-standard model interaction must be explained by any complete model, which may also require a tuning of parameters.

In this chapter I will introduce a promising model for dark matter interactions with the standard model: Kinetic Mixing. Kinetic mixing (KM) is a phenomenon that produces an interaction between gauge bosons of two different gauge groups, and generically occurs when there are two U(1) gauge symmetries in a theory. KM between abelian gauge groups occurs via a renormalizeable operator, and KM between

[1]This chapter is based on reference [21] written in collaboration with Spencer Chang and Chris A. Newby and unpublished work done in collaboration with the two aforementioned and Bryan M. Ostdiek.

any two gauge groups will be generated by loop processes whenever there are particles charged under both symmetries [14, 69].

The reason kinetic mixing is attractive as a model for dark matter interactions is that the mixing parameter, and hence the interaction strength, can easily be made small. The rate of interaction between the dark matter and the standard model scales as the square of the mixing strength, which we denote by ϵ, and if kinetic mixing is generated by, for example, processes at the GUT scale, the mixing parameter will be around $\epsilon \sim 10^{-6} - 10^{-4}$ [70]. Kinetic mixing's naturalness as an ingredient in BSM models makes it a hotly studied phenomenon. For example, in Z' [69][2] as well as many dark matter models [15, 71], the SM is supplemented by an additional U(1) gauge symmetry which can mix with $U(1)_Y$. These models have in turn motivated a large and diverse experimental effort with current and upcoming searches at intensity frontier experiments (fixed-target and flavor factories) and the LHC (see [72] for overview and references).

One topic which is not often discussed is the fact that, in most cases, there is an additional ingredient required to generate kinetic mixing: another particle which is charged under both the involved gauge forces, and which mediates kinetic mixing. The details of this particle and it's role in kinetic mixing will be discussed in detail below. In this chapter I will focus on the properties of this mediating particle. The main focus of the aforementioned searches and models has been on the dynamics of the dark photon itself, or signals of particles charged only under the dark sector, while little attention has been paid to the mediating particle. The reason this mediating

[2]A Z' is a new, heavy, gauge boson with mass comparable to the Z of the standard model. In this chapter I will focus on much lighter bosons, in the 100s of MeV mass range.

particle is ignored is that it's mass can usually be made large while leaving the KM strength fixed. In the most studied case of KM between two abelian sectors, where the mixing operator is dimension four, the mediator mass only logarithmically affects the strength of KM. Moreover, KM between abelian sectors is described by a renormalizable operator, so it can be included without explicit reference to a mediator. Thus, in the abelian case, it is not guaranteed that the mediator will be light enough to be discovered. On the other hand, when KM goes through a nonabelian gauge sector, the operator is nonrenormalizable and thus inextricably linked to a mass scale. This fact gives nonabelian kinetic mixing models unique predictive power which has not yet been studied in the literature. This work fills that gap. Furthermore, as this work shows, nonabelian KM strengths relevant for current intensity frontier experiments are unambiguously linked to a weak scale mediator, predicting a correlated signal at the energy frontier. Although such nonabelian mixing is already well known in the literature this study represents the first statement of this connection, and the first presentation of a model where a nonabelian operator is the sole origin of KM.

Kinetic Mixing

To begin I will introduce kinetic mixing, it's historical context, and its generalization to nonabelian gauge fields.

Kinetic mixing was first introdiced in 1985 by Holdom [14]. It was recognized that kinetic mixing between two abelian gauge symmetries arises from a renormalizeable operator meaning that it should generically occur in a Lagrangian with order one coefficient. This term is of the form

$$\frac{\epsilon}{2} F_{\mu\nu} F_D^{\mu\nu} \tag{3.1}$$

Where $F_D^{\mu\nu}$ is a new abelian gauge field strength, $F_{\mu\nu}$ is a standard model field strength, and ϵ is the strength of kinetic mixing. Of course, there is not such mixing with order one coupling in our universe, but we will return to that point in a moment, however we will assume for the remainder of this discussion that ϵ is small.

Once this interaction is introduced into the Lagrangian, it is convenient to introduce a field redefinition to remove this kinetic mixing term:

$$A^\mu \to A^\mu + \epsilon A_D^\mu \tag{3.2}$$

$$A_D^\mu \to A_D^\mu - \epsilon A^\mu \tag{3.3}$$

where A (A_D) denotes the gauge field associated with the standard model (dark) gauge symmetry and which (to leading order in ϵ) removes the kinetic mixing term. Of course, the mixing term can be removed to all orders in ϵ, but this is good enough for our purposes. Notably, this field redefinition also introduces a coupling to the new gauge field to particles charged under the standard model. To see this, consider what happens to the minimal gauge coupling of a charged particle to the standard model field strength A^μ under this field redefinition.

$$q A^\mu \bar{\psi} \gamma_\mu \psi \to q \left(A^\mu + \epsilon A_D^\mu \right) \bar{\psi} \gamma_\mu \psi = q A^\mu \bar{\psi} \gamma_\mu \psi + \epsilon q A_D^\mu \bar{\psi} \gamma_\mu \psi \tag{3.4}$$

so that the particle charged under a standard model gauge field which undergoes kinetic mixing can be considered to develop a "millicharge" under the new gauge field, with charge ϵq. This phenomenon makes kinetic mixing a useful model building tool, especially for coupling dark sectors to the standard model since the resulting interaction strength is naturally very weak. Additionally, it is promising from a phenomenological perspective, because it means that the dark photon will be able to decay into, for example, electrons. Of course, there is still the issue of why ϵ is not order 1. This is the topic we discuss next.

Since this coupling does not appear as order one in nature, the next most natural conclusion is that it is zero. However, even if the coupling is zero for the full theory of the universe, it can become nonzero at low energies. The way this occurs is by heavy particles which are charged under both of the gauge symmetries being "integrated out" and generating this interaction as part of an effective field theory (for details on effective field theory see any modern reference, for example [73]). This particle that is integrated out to generate kinetic mixing is called the mediator. If there is a mediator with electromagnetic charge, and charge under a new abelian gauge symmetry, at energies much less than its mass (where it can be integrated out) the heavy particle will generate kinetic mixing from a loop process with coupling

$$\frac{c\log(m_\phi/\Lambda)}{4\pi}F_D^{\mu\mu}F_{\mu\nu} \tag{3.5}$$

where m_ϕ is the mediator mass, c is a constant, Λ is the renormalization scale (for example, a the LHC one might use $\Lambda \sim 13\,\text{TeV}$) and 4π indicates that this is a loop in the process, which makes the coupling naturally weak. We refer to this heavy particle as "the mediator". The fact that the mediator mass only contributes

logarithmically to this interaction is a consequence of the fact that this term is itself renormalizeable. One notable consequence of this is that the strength of this interaction gives essentially no information about the mass of the mediating particle. The situation is very different in nonabelian kinetic mixing.

When kinetic mixing occurs between an abelian and a nonabelian gauge field, the situation is very different. In particular, the nonabelian gauge field strength has an additional gauge index. Hence, the analogous term to Eq. 3.1 would not be gauge invariant. In order to make the mixing term gauge invariant, additional fields need to be introduced. Introducing the operator $\mathcal{O}^a$, which we assume has the appropriate gauge structure to make the term gauge invariant, allows us to build a term in the Lagrangian of the form

$$\mathcal{L}_{NAKM} \supset \frac{\mathcal{O}^a}{\Lambda^n} F_{D\mu\nu} W_a^{\mu\nu} \tag{3.6}$$

where now $W_a^{\mu\nu}$ is the field strength of a nonabelian gauge field, a is the associated gauge index, and n is the mass dimension of $\mathcal{O}^a$. In order to keep this term dimensionally correct we add a factor $1/\Lambda^n$. This interaction now describes a vertex with two gauge bosons and whatever fields have gone into constructing $\mathcal{O}^a$. In order to generate kinetic mixing the operator $\mathcal{O}^a$ must develop a vacuum expectation value. This spontaneously breaks the gauge symmetry associated with W^a, and generates kinetic mixing. To this end, taking the vacuum expectation of $\langle \mathcal{O}^a \rangle = v^n \delta_i^a$, where i is the direction in gauge space picked out by spontaneous symmetry breaking, gives the kinetic mixing operator:

$$\mathcal{L}_{NAKM} \supset \frac{v^n}{\Lambda^n} F_{D\mu\nu} W_i^{\mu\nu} \equiv \frac{\epsilon}{2} F_{D\mu\nu} F^{\mu\nu} \tag{3.7}$$

Where ϵ is again the kinetic mixing strength and here $F^{\mu\nu} = W_i^{\mu\nu}$. From the point of view of effective field theory, we should interpret Λ as the mass scale of some new physics that has been integrated out, in this case the mediator. To that end we write $\Lambda = 4\pi m_\phi / c$ where m_ϕ is the mass of the mediator, c is an order 1 coupling associated with this new physics, and we include a loop factor of 4π as will generally appear when such interactions are generated by loop processes. Plugging this into Eq. 3.7 shows that nonabelian kinetic mixing predicts a new particle with mass:

$$m_\phi = \frac{v}{4\pi c}\epsilon^{-1/n} \tag{3.8}$$

Nonabelian Kinetic Mixing in the Standard Model

In this work we discuss a case of particular modern interest: an abelian dark sector mixing with $\mathrm{SU}(2)_L$ of the SM. The lowest dimensional operator involving only SM fields and the dark photon which kinetically mixes $\mathrm{SU}(2)_L$ and the dark photon is

$$\frac{c}{16\pi^2 m_\phi^2}\left(H^\dagger \tau^a H\right) W^a_{\mu\nu} F_D^{\mu\nu} \tag{3.9}$$

where $W^a_{\mu\nu}(F_D^{\mu\nu})$ is the field strength of the SM $\mathrm{SU}(2)_L$ gauge boson (dark gauge boson), H is the SM higgs field, and τ^a are the Pauli matrices divided by two. Anticipating the origin of this operator, we include the mass of the mediator m_ϕ, a loop factor, and absorb $O(1)$ numbers and couplings into the coefficient c. Once electroweak symmetry is broken, Eq. 3.9 contains the canonical mixing between the photon and the dark photon

$$\frac{\epsilon}{2} F_{\mu\nu} F_D^{\mu\nu}; \qquad \epsilon = \frac{c\, v^2 s_W}{32\pi^2 m_\phi^2} \tag{3.10}$$

where s_W is the sine of the electroweak mixing angle, and v is the SM higgs vacuum expectation value (vev). Already this expression shows a connection between intensity and energy frontier experiments: planned searches for the dark photon include *i*) fixed target experiments, probing the region $\epsilon \sim 10^{-5} - 10^{-4}$ for a dark photon of mass $M_{A_D} \sim 10 - 200$ MeV and $\epsilon \gtrsim 3 \times 10^{-4}$ for $M_{A_D} \sim 10 - 600$ MeV (*e.g.* APEX [74] and HPS [75]), *ii*) next generation flavor factories, sensitive to $\epsilon \sim 10^{-4} - 10^{-3}$ for dark photon masses up to 10 GeV [72] (going beyond existing BABAR, BESIII limits [76, 77]), and *iii*) a proposed LHCb search sensitive to the range $\epsilon \sim 10^{-5} - 10^{-3}$ and $M_{A_D} \leq 100$ MeV [78]. In our models of interest, Eq. 3.11 shows that this parameter space requires

$$m_\phi = \sqrt{\frac{c\, v^2 s_W}{32\pi^2 \epsilon}} \sim \sqrt{\frac{c}{\epsilon/10^{-4}}} \times 1\,\text{TeV}. \tag{3.11}$$

Thus, in theories with only nonabelian kinetic mixing, there is a strong correlation between signals of dark photons at the intensity frontier and the corresponding mediator particles at the LHC. This conclusion is independent of the specific realization of nonabelian KM.

In the rest of this paper we present a simple model where the only KM that occurs is nonabelian. In such scenarios, the mediator particle's signals at the LHC are correlated with the dark photon searches of the intensity frontier. We will analyze the model's dynamics and then discuss the mediator particle's phenomenology and relevant constraints.

Nonabelian Kinetic Mixing Model

In this model, there is a dark gauge symmetry $\text{U}(1)_D$ with a dark photon, A_D. The field mediating KM is a scalar $\text{SU}(2)_L$ triplet with unit dark charge that we call ϕ. In order to give the dark photon mass we introduce a dark higgs, H_D, with unit

dark charge that gets a vev $\langle H_D \rangle = v_D/\sqrt{2}$. The most general, renormalizable theory with these fields has many terms in its scalar potential. Only a subset of them will be relevant for our discussion, and the terms we study are

$$\begin{aligned} V(H, H_d, \phi) &= \lambda|H|^4 - \mu^2|H|^2 + \lambda_D|H_D|^4 - \mu_D^2|H_D|^2 \\ &\quad + m_\phi^2|\phi|^2 + \lambda_{\rm mix}(\phi^\dagger T^a \phi)(H^\dagger \tau^a H) \\ &\quad + \kappa\left[\phi^a (H^\dagger \tau^a H) H_D^\dagger + \text{h.c.}\right] \end{aligned} \tag{3.12}$$

where κ can be taken to be real after a field redefinition and T^a is the triplet representation's generators for $\text{SU}(2)_L$. Of particular importance is the term with coefficient $\lambda_{\rm mix}$ as it is responsible for KM. After integrating out ϕ, KM is generated with strength

$$\epsilon = \frac{g g_D \lambda_{\rm mix}}{96\pi^2} \frac{v^2}{m_\phi^2} s_W \sim 10^{-4}\, g_D\, \lambda_{\rm mix} \left(\frac{400\ \text{GeV}}{m_\phi}\right)^2 \tag{3.13}$$

where g is the gauge coupling for $\text{SU}(2)_L$, and g_D is the dark gauge coupling. As the final expression shows, if the new couplings are order one, mixings relevant to intensity frontier experiments are spanned by m_ϕ in the range 100 GeV $-$ 1 TeV.

This model does not contain a particle charged under both $\text{U}(1)_D$ and hypercharge so there is no abelian kinetic mixing. If, for example, this model were embedded into a grand unified theory (GUT), particles with GUT-scale masses may generate abelian kinetic mixing, however in that case abelian kinetic mixing would arise from two-loop diagrams and would generate mixing strengths on the order $\epsilon \sim 10^{-6} - 10^{-4}$ as discussed in [70]. In this model nonabelian kinetic mixing is dominant over, or of comparable strength to, abelian mixing. This means that we can use Eq. 3.13 to predict the mediator mass from the kinetic mixing strength.

mass spectrum

The term responsible for KM also generates a mass splitting in the ϕ states. Two states, labeled $\chi^{\pm}$ and $\eta^{\pm}$, are charged under electromagnetism and have masses

$$m_\chi^2 = m_\phi^2 + \frac{\lambda_{\rm mix} v^2}{4}, \quad m_\eta^2 = m_\phi^2 - \frac{\lambda_{\rm mix} v^2}{4}. \tag{3.14}$$

This splitting can cause the lightest charged state's mass to become tachyonic, spontaneously breaking $\mathrm{U}(1)_{EM}$ and giving the photon mass. This places a constraint that $m_\phi^2 > \lambda_{\rm mix} v^2/4$.

The two remaining, neutral degrees of freedom are the real and imaginary parts of the third component of ϕ, denoted ϕ_R^0 and ϕ_I^0, respectively. These states will be nearly degenerate with mass m_ϕ – a very small splitting is generated which vanishes as $\kappa \to 0$. Throughout we will use ϕ to refer to all of these states collectively and their individual names when specificity is required.

Potential Minimization

The κ term in the potential was introduced in order for the ϕ particles to decay, but also has other important effects that can constrain the model. Once the electroweak and dark symmetries are broken, this term induces a vev for the real, neutral component of ϕ. The size of this vev is

$$\langle \phi \rangle = \frac{\kappa v^2 v_D}{4\sqrt{2} m_\phi^2}. \tag{3.15}$$

Since this is only in the neutral component, $\mathrm{U}(1)_{EM}$ remains unbroken, but it does shift the W boson mass, with a contribution to the T parameter

$$T_{\langle\phi\rangle} \sim 10^{-3}\,\kappa^2 \left(\frac{v_D}{1\ \mathrm{GeV}}\right)^2 \left(\frac{200\ \mathrm{GeV}}{m_\phi}\right)^4, \tag{3.16}$$

which is very small as long as the dark photon scale is sub-GeV. In addition, there is a one loop contribution to T from the ϕ particles due to their mass splitting [79] which in the limit of small splitting goes as

$$T_{\mathrm{loop}} \sim \frac{\lambda_{\mathrm{mix}}^2 v^4}{192\pi s_W^2 c_W^2 m_Z^2 m_\phi^2} \sim 0.1\,\lambda_{\mathrm{mix}}^2 \left(\frac{200\ \mathrm{GeV}}{m_\phi}\right)^2. \tag{3.17}$$

Contributions to S are negligible, so to be consistent with electroweak precision constraints requires $T < 0.2$ (95% C.L.) [80], putting a lower bound on m_ϕ (from Eq. 3.17) and an upper bound on κ (from Eq. 3.16).

The κ term also causes mixing between ϕ_R^0, h_D, and the SM higgs. This leads to a correction to the μ_D^2 term of size $\kappa^2 v^4/(16 m_\phi^2)$. Thus, a large hierarchy between the dark and electroweak scales requires a tuning in the value of μ_D^2. The severity of this tuning depends on κ, and for certain regions of parameter space this tuning can be small. It is however interesting that the tuning in this model is indirectly observable. This is in contrast to the SM where the details of tuning depend on some unknown, as-of-yet-unobservable higher scale. If KM with $SU(2)_L$ is observed, this model will provide insight into the validity of tuning as a theoretical constraint.

Fixed Target Benchmark

Now lets consider a benchmark set of parameters, chosen in order to remain within the region of immediate interest to fixed-target experiments: $m_{A_D} = 0.1$ GeV and $g_D = 0.5$. This choice implies that $v_D = 0.2$ GeV, and we set $m_{h_D} = 0.4$ GeV so that the dark higgs can decay into two dark photons. Note that the dark higgs and photon masses are negligibly small relative to electroweak scale masses, so we can safely neglect them in later formulas. We also set $\lambda_{\text{mix}} = 1$ which puts a lower limit on m_ϕ of 155 GeV due to the electroweak precision constraint. In our analysis we specifically explore the range 150 GeV $< m_\phi <$ 500 GeV in order to be relevant for collider searches while remaining in the $10^{-5} < \epsilon < 10^{-3}$ window, though it should be kept in mind that precision electroweak constraints exclude the small part of this region $m_\phi <$ 155 GeV.

Decays

A ϕ particle can decay directly into gauge and higgs bosons through the κ term, or undergo cascade decays through its mass states by radiating $W^{(*)}$ bosons. The cascade decay rate, in the large m_ϕ and massless fermion limit, is

$$\Gamma(\chi^\pm \to W^{\pm *}\phi^0_{R,I}) = \Gamma(\phi^0_{R,I} \to W^{\mp *}\eta^\pm) = \sum_{f\bar{f}'} \frac{N_c G_f^2 \Delta m^5}{15\pi^3} \tag{3.18}$$

where G_f is the Fermi constant, Δm is the mass splitting between ϕ states, and $f\bar{f}'$ includes all fermion pairs except the top-bottom pair for which the splitting Δm is too small to produce. The κ mediated decay rates, in the limit that $m_{h_D}, m_{A_D} \to 0$,

are

$$\begin{aligned}
\Gamma(\phi_R^0 \to h h_D) &= \Gamma(\phi_I^0 \to h A_D) = \frac{\kappa^2 v^2}{64\pi m_\phi^3}\left(m_\phi^2 - m_h^2\right), \\
\Gamma(\chi^\pm \to W^\pm h_D) &= \Gamma(\chi^\pm \to W^\pm A_D) \\
&= \frac{\kappa^2 v^2}{128\pi m_\phi^4 m_\chi^3}\left(m_\chi^2 - m_W^2\right)^3, \text{ and} \\
\Gamma(\eta^\pm \to W^\pm h_D) &= \Gamma(\eta^\pm \to W^\pm A_D) \\
&= \frac{\kappa^2 v^2}{128\pi m_\phi^4 m_\eta^3}\left(m_\eta^2 - m_W^2\right)^3.
\end{aligned} \tag{3.19}$$

The decay phenomenology depends sensitively on κ. If κ is sufficiently small the cascade decays will dominate, and heavier ϕ will tend to decay down to the lightest state, $\eta^\pm$, emitting two fermions via an off-shell W per step, followed by the $\eta^\pm$ decaying half the time to $W^\pm h_D$ and half the time to $W^\pm A_D$. On the other hand, if κ is large, κ mediated decays dominate with the neutral components of ϕ decaying as $\phi_R^0 \to h h_D, \phi_I^0 \to h A_D$ and $\eta^\pm, \chi^\pm$ decaying to $W^\pm h_D, W^\pm A_D$ equally. Note that the simplicity of the decays are a consequence of our benchmark choice. As the value of v_D is increased from our benchmark, additional decay modes due to κ become more important, *e.g.* $\phi_R^0 \to hh, ZZ, WW$ and $\eta^\pm \to W^\pm h, W^\pm Z$. However, since these decay rates are proportional to v_D^2, only when $v_D \gtrsim 100$ GeV do these start to become important and thus in the intensity frontier parameter space we do not expect these decays to have appreciable rates.

In Fig. 10, we highlight some of the important regions of our benchmark parameter space. Some characteristic values of ϵ are given at three m_ϕ values in dashed lines, though these can be scaled up or down by changes in $g_D, \lambda_{\rm mix}$. The green line denotes the value of κ where the cascade decays are comparable to the κ induced decays below which the off-shell cascade decays dominate. The middle region

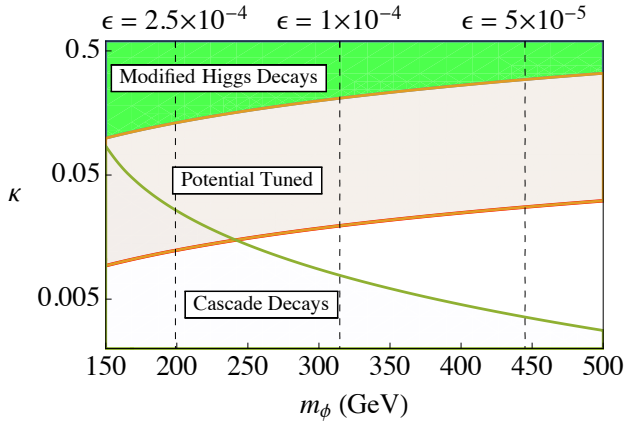

FIGURE 10. This figure shows regions of interest in the (m_ϕ,κ) plane. Starting from the top, the regions are where the new higgs decays are greater than 10% of its SM expected total width (green region), where μ_D^2 is tuned to $> 10\%$ (above the thick orange curve) and where the electroweak cascade decays are faster than the κ decays (below the green curve). Vertical dashed lines mark values of ϵ, labeled at the top.

of Fig. 10 shows where the tuning in μ_D^2 is worse than 10%, and the last region at the top shows when the SM higgs has new decays with a branching ratio greater than 10%, which will be discussed below.

Production Rates: In order to observe these decays, ϕ particles will need to be produced, which at a hadron collider proceeds predominantly through Drell-Yan production. The production cross sections at the 13 TeV LHC are shown in Fig. 11. We used FeynRules [81] to generate our Lagrangian and CalcHEP [82] to generate the events using the `cteq6l` parton distribution function for the proton. Pair production of the neutral particles does not occur due to the lack of photon, Z couplings. Also, production rates for ϕ_I^0 are identical to ϕ_R^0 and so are not included on the plot.

The strategy for ϕ searches should start with adaptations to the existing searches for dark photons and lepton jets [70, 83–85]. All events contain either h_D or A_D particles produced at significant boosts, which coupled with the decay $h_D \to A_D A_D$, will lead to many events with boosted lepton pairs. For small enough ϵ, many of

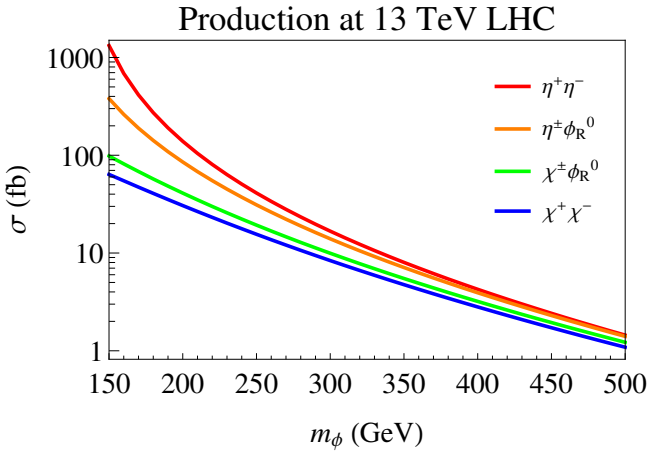

FIGURE 11. This figure shows the pair production cross section for various mass states of ϕ at the $\sqrt{s} = 13\,\text{TeV}$ LHC. The different curves are: two η states (red), an η and a ϕ_R^0 or ϕ_I^0 (orange) a χ and a ϕ_R^0 or ϕ_I^0 (green) and two χ states (blue). The legend is arranged in order of decreasing cross section. Curves were generated using the `cteq6l` parton distribution function of CalcHEP [82].

these A_D decays will be displaced. If the value of κ is small, where cascade decays dominate, there will also be soft leptons or jet activity from the off-shell W's. An interesting signal in this regime is the possibility of same sign η production due to the cascade decays of ϕ_R^0, ϕ_I^0 going equally into $\eta^\pm$ (see Eq. 3.18). Their subsequent decay produces a like-sign pair of W's leading to same sign lepton events in addition to the lepton jets of the event. On the other hand, if the value of κ is large, there can be other associated objects like the SM higgs bosons produced in ϕ_R^0, ϕ_I^0 decays (see Eq. 3.19), which could be of interest in terms of tagging or reconstructing the events. To summarize, this scenario's predominant collider signal is lepton jets in association with W, h with mass resonances between a lepton jet and the W or h.

Since the benchmark's dark photon mass restricts it to electron decays, the lepton jets could be challenging to pick out. Boosted electron pairs are much more difficult to distinguish from jets and in fact, most existing lepton jet searches rely on muons

(with significant constraints only for $M_{A_D} > 2m_\mu \sim 0.2$ GeV). To overcome these challenges, some promising strategies could be to look for displaced jets and/or jets with significant electromagnetic energy deposit. We leave studies of such issues as well as existing LHC constraints and discovery reach for such particles to future work.

SM Higgs Phenomenology

This model also predicts new decays for the SM higgs. The dominant new decays are into dark higgs bosons and dark gauge bosons. The kinetic mixing operator itself, Eq. 3.9, generates new decays of the higgs to a dark photon and either a Z or a photon. The rates of these decays are

$$\Gamma(h \to h_D h_D) = \Gamma(h \to A_D A_D) = \frac{\kappa^4 v^6}{512\pi m_h m_\phi^4} \tag{3.20}$$

$$\Gamma(h \to \gamma_D \gamma) = v\frac{\epsilon^2}{32\pi}\left(\frac{m_h}{v}\right)^3 \tag{3.21}$$

$$\Gamma(h \to \gamma_D Z) \cong \Gamma(h \to \gamma_D \gamma) \times \left(\frac{2\, c_W}{s_W}\right)^2 \times 10^{-1} \tag{3.22}$$

again we take the limit where A_D and h_D are massless. Indirectly, these new decay widths are constrained by the relatively good fits of the SM higgs decay signal strengths [86]. As an approximation of this constraint, the top green region of Fig. 10 shows where higgs decays into the dark sector exceed 10% of the SM higgs total width. In particular, decays of the higgs involving the dark photon are a direct consequence of the kinetic mixing term, and provide a model independent signal of nonabelian kinetic mixing. For $\epsilon \sim 10^{-3}$ the branching ratio of the higgs to a dark photon will be $\Gamma(h \to \gamma_D + Z/\gamma) \sim .5 \times 10^{-6}$ GeV. There is potential for the LHC to detect these higgs decays, if the dark photon is heavier than our benchmark. For example, if $m_{A_D} \sim 0.6 - 60$ GeV, the LHC can be sensitive to the dark photon through higgs

decays into $2A_D$ [87] and a recent LHC analysis constrains $Br(h \to 2A_D) \gtrsim 3 \times 10^{-4}$ for $m_{A_D} = 15 - 60$ GeV [88]. While the fixed target parameter space motivates searches at much lower dark photon masses, a simple modification of our benchmark can give these heavier masses. In these modified benchmarks, if one improves the higgs branching ratio constraint to $BR_{\text{new}} < BR_{\text{limit}}$, this would constrain the range $\kappa > 0.25(m_\phi/200 \text{ GeV}) Br_{\text{limit}}^{1/4}$. As our formulas and discussion show, increasing m_{A_D} to these larger values, either through increasing g_D or v_D, changes very little in the ϕ phenomenology, however, in this heavier parameter space correlated signals at the intensity frontier could only be seen at future flavor factories for $m_{A_D} < 10$ GeV.

Collider Study

There are three potentially striking collider signatures of the model we present here[3]: prompt and displaced lepton jets, same sign leptons, and resonance features associated with production of the mediator. Searches have already been done in search of lepton jets and same sign leptons [85, 89, 90]. Relevant same sign lepton searches done already are optimized to search for standard model processes producing same sign leptons and are relatively ineffective for constraining this model. Displaced lepton jet searches loose sensitivity because in order to make ϵ sufficiently small to displace a lepton jet generically requires that m_ϕ be large, which lowers the mediator production cross section substantially. On the other hand, the model considered here produces prompt lepton jets at low mediator masses, where the production rate is relatively large. As a result, prompt lepton jet searches are able to meaningfully constrain the parameter space of this model. I will detail our approach below, and

[3]The work presented in this section is unpublished work done in collaboration with Chris A. Newby, Spencer Chang, and Bryan M. Ostdiek

then discuss possibilities for improving search methods in future analyses.

Prompt Lepton Jet Analysis

The ATLAS search for prompt lepton jets detailed in [85] relies on dark photons, or scalars which couple to dark photons, being produced in collision events which subsequently decay into pairs of leptons. The results are thus somewhat dependent on the dark photon production mechanism. In our model dark photons are produced as the end state of mediator pair production and subsequent decay, which makes the mediator mass a significant factor in constraining our model. We reapply this prompt lepton jet analysis to simulated events generated according to our model. As I will show below, this analysis already constrains significant regions of nonabelian kinetic mixing parameter space, but there is much room for improvement.

Our simulation environment uses FeynRules [81] to generate the model file, MadGraph5 [91] to simulate parton-level events, Pythia [92] to simulate decays, and Delphes [93] to simulate the detector response. Lepton jets are reconstructed following the procedure detailed in [85] with the one modification that, instead of requiring a reconstructed electron in a lepton jet as specified for electron lepton jets (section 5.2 in [85]), we instead require a track whose truth-level particle ID is that of an electron in the lepton jet. This is because we find that Delphes always reconstructs the electrons in the lepton jet as a single jet object, never registering an isolated electron. We assume that electron reconstruction by the experimental collaborations will be better able to reconstruct electrons appropriately. Indeed, it is reported that in the original analysis electron lepton jets were usually reconstructed as a single electron, instead of

as a jet. This choice may overestimate our signal events by a small factor, simulating our lepton jet reconstruction efficiency and comparing to Figure 5 of [85] matches quite well, reassuring us that our reconstruction is accurate.

In the original analysis of [85] additional cuts are applied to remove background, which is primarily from multijet and W-plus-jets events, of which multijet is dominant. Some of the cuts applied are infeasible in our simulation invironment. We were able to simulate the isolation cut and a cut on the fraction of energy deposited in the electromagnetic calorimeter (EM frac.). The other cuts may have a slight effect on signal efficiency, but it is noted in the original analysis that the primary effect of these additional cuts is to reduce background and only slightly reduce signal efficiency. The isolation variable can easily be computed using simulated tracks according to the procedure detailed in the original analysis. In order to compute the EM frac. variable we use the delphes variable 'EhadOverEem' of the nearest reconstructed jet to each lepton jet, which is quite accurate since almost all of the lepton jets are reconstructed as jets by Delphes. To compute EM frac. we use the relationship

$$\text{EM frac} = \frac{1}{1 + \text{EhadOverEem}} \tag{3.23}$$

The effectiveness of this analysis on any given parameter point is controlled by two primary variables: the cross section, which controls how many events are available, and the dark photon decay length, which controls whether the resulting lepton jets are prompt, or not. For our benchmark scenario, $m_{A_D} = .1$ GeV, the decay length is approximately:

$$L_{\text{decay}} \sim (10^{-11}\text{meters}) \times \epsilon^{-2} \times \frac{m_\phi^2 - m_W^2}{2 m_\phi m_{A_D}} \tag{3.24}$$

Here, the final factor is approximately the boost of the dark photon. In order to be "prompt" as defined by the original analysis a lepton jet must have an impact parameter $d_0 < 1.5 \times 10^{-3}$ meters from the beam pipe, meaning that signal efficiency starts to drop significantly for $\epsilon < \times \sqrt{(m_\phi^2 - m_W^2)/(m_\phi m_{A_D})} 10^{-5}$. For our benchmark scenario, in which the relationship between m_ϕ and ϵ is explicit, this works out to be $\epsilon \lesssim 5 \times 10^{-4}$, in order to probe lower ϵ will require quite high luminosity.

In order to get a meaningful sampling of parameter space, we simulated events with parameters in the $m_\phi - \epsilon$ plane in the region 150 GeV $< m_\phi <$ 350 GeV and $10^{-5} < \epsilon < 10^{-3}$. We use the parameters of our benchmark excepting λ_{mix} which we vary in order to achieve the desired relationship between m_ϕ and ϵ. To get a flavor for the varied phenomenology of this model, we study two values of κ; one "low kappa" region in which $\kappa = .001$ and cascade decays dominate, and a "large kappa" region in which $\kappa = .05$ and kappa decays dominate. This work is still in progress but, preliminarially, we find that parameter space is constrained by this analysis for $\epsilon \gtrsim 2 \times 10^{-4}$, as shown in Fig. 12, with slight differences arising for low and large κ.

Of particular note is the shift in constraint of the low m_ϕ region between low and large κ. In particular the low κ scenario is somewhat more weakly constrained. This is because in the low m_ϕ region of parameter space the mass of the lightest state (η) can become very close to the W mass, which in turn limits the P_t of the final state dark photons. Since lepton jets are required to have $P_t > 20$ GeV by the analysis, this significantly weakens constraints in the low κ, low m_ϕ region of parameter space, where almost all of the mediators produced will undergo a cascade of decays to the

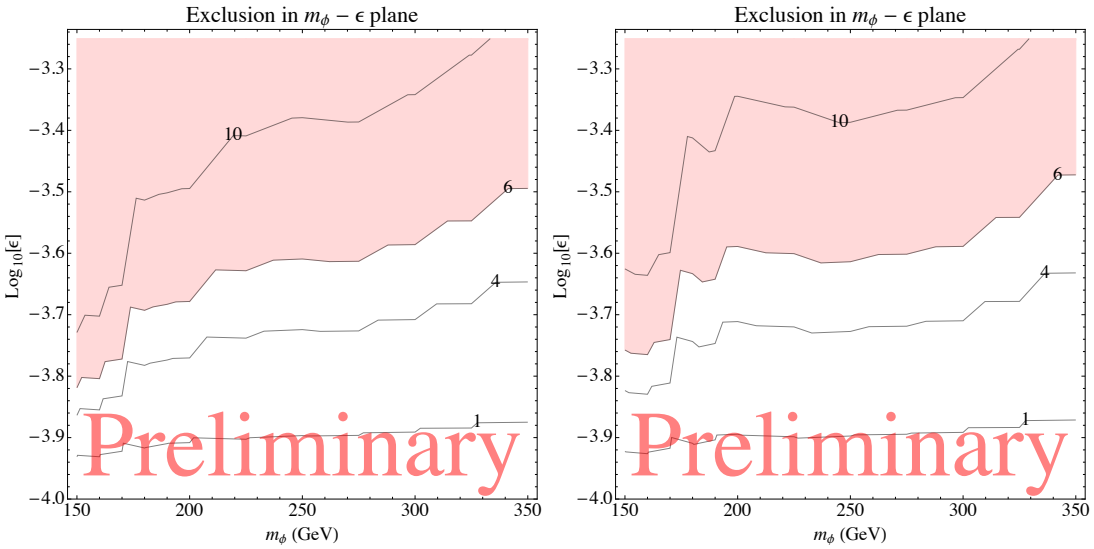

FIGURE 12. Exclusions of our model in the m_ϕ - ϵ plane from a prompt lepton jet search with $20 fb^{-1}$ of LHC data. Our large κ benchmark is $\kappa = .05$ and the low kappa benchmark is $\kappa = .001$. Shaded regions are excluded at the 95% C.L. and contour labels denote the expected number of events.

lightest state and produce relatively soft lepton jets.

Future Directions

Certainly there is more work to be done in analyzing the collider signatures of this model, and a detailed collider study is in preparation, however already we can see that current analyses are constraining the relevant parameter space. There is hope to constrain additional parameter space at higher luminosity, where there may be significantly more signal events. Unfortunately, the multijet backgrounds will scale similarly as the signal with luminosity. The constraints on this model at high luminosity could be significantly improved with better background rejection. An effective way to reject additional background for this model is to additionally require a hard, isolated lepton in the event from the W bosons associated with mediator decay.

A W boson decays leptonically approximately 1/3 of the time, so with two W bosons in the event (one from each mediator) we expect an additional reduction in signal efficiency of approximately 50%. On the other hand, this requirement will reduce the dominant multijet background by at least a factor of the lepton fake-rate, which is around 10^{-2} [94]. It may even be that this requirement will make W plus jets the dominant background in the analysis. Unfortunately this approach will not improve limits using the current data set since the search has almost zero backgrounds as is. Even with zero backgrounds, the 95% C.L. limit is ~ 3 expected events, which is only half the 95% CL limit with multijet backgrounds. On the other hand, with higher luminosity this strategy will significantly improve the sensitivity of this search. A more detailed analysis of this strategy is forthcoming.

Conclusions

In this letter, we have argued for a direct connection between current intensity frontier searches for dark photons and the signals of new particles at the LHC. The connection occurs if KM involves a nonabelian gauge symmetry, since the mixing operator requires higgs fields to be gauge invariant and thus closely ties the mediator particle mass to the vev of the higgs and the strength of KM. To illustrate this, we wrote down a simple model where the only KM which occurs is between a new dark U(1) gauge symmetry and $SU(2)_L$. This requires a scalar triplet ϕ of $SU(2)_L$ which is charged under the dark U(1). Analyzing the model, we looked at the constraints and briefly considered the phenomenology of the ϕ particles at the LHC which could be searched through simple modifications of existing dark photon searches. We showed that modern prompt lepton jet searches already constrain some regions of parameter

space. We also argued for a search strategy involving an additional hard lepton, in order to reduce multijet backgrounds.

Aside from our simple model, there are obvious extensions to explore. Fermionic mediators, mixing with a nonabelian dark gauge symmetry and incorporating dark matter are all intriguing modifications, which will all produce the same, model-independent correlation of signals. Interestingly, these directions all tend to lead to larger multiplicity in the dark sector, suggesting that the model in this paper is unique in its simplicity. Investigation of these directions, as well as a detailed collider study of this model is forthcoming.

To conclude, KM of the $\mathrm{SU}(2)_L$ of the SM and an abelian dark sector is timely and well motivated given the current run of the LHC, ongoing fixed target experiments, and potential next generation flavor factories. The connection it draws between intensity and energy frontier experiments is unambiguous and leads to correlated signals at these experiments, promising unprecedented insight into the physics of the dark sector.

APPENDIX A

DERIVATION OF NONRELATIVISTIC OPERATORS

As mentioned earlier, there are two ways of constructing the velocity degrees of freedom used in our nonrelativistic theory: starting with Galilean invariant operators and orthogonalizing them or starting with the relativistic kinematics and reducing to the nonrelativistic limit. Here we derive the results shown in section 2.1 using the second method.

To begin, we have the four four-momenta of Fig. 1 from which we need to construct Galilean invariant velocities. As there are ten constraints; one from energy conservation, three from momentum conservation, four from mass constraints, and two from rotational invariance; we only need two velocity operators. Using a little foresight, we define three velocities

$$\begin{aligned} \vec{v}_N &\equiv \vec{v}_{N_{in}} - \vec{v}_{N_{out}}, \\ \vec{v}_\chi &\equiv \frac{m_{\chi_1} + m_{\chi_2}}{2m_N}(\vec{v}_{\chi_2} - \vec{v}_{\chi_1}), \text{ and} \\ \vec{v}_{\rm el}^{\perp} &\equiv \frac{1}{2}(\vec{v}_{\chi_2} + \vec{v}_{\chi_1} - \vec{v}_{N_{out}} - \vec{v}_{N_{in}}). \end{aligned} \tag{A.1}$$

and expect to find one relationship between them beyond the orthogonality relations so as to have a total of six degrees of freedom. The mass factor in front of the relative DM velocity is so that in the elastic limit $\vec{v}_\chi \to \vec{v}_N$. We also chose the form for $\vec{v}_{\rm el}^{\perp}$ which is perpendicular to the momentum transfer in the elastic limit and because the velocities have good quantum numbers under P, T, and hermitian conjugation.

Now that we have our three velocities, we need to orthogonalize them. We begin with Lorentz invariant combinations:

$$
\begin{aligned}
(p+k)^2 &= (p'+k')^2, \\
(p-k')^2 &= (p'-k)^2, \\
k'^2 &= (p+k-p')^2, \text{ and} \\
(p-p')^2 &= (k-k')^2,
\end{aligned}
\tag{A.2}
$$

which we take the nonrelativistic limit of to obtain

$$
\begin{aligned}
&-(m_{\chi_1}+m_N)^2 - m_{\chi_1}m_N(\vec{v}_{\chi_1}-\vec{v}_{N_{in}})^2 = -(m_{\chi_2}+m_N)^2 - m_{\chi_2}m_N(\vec{v}_{\chi_2}-\vec{v}_{N_{out}})^2, \\
&-(m_{\chi_1}-m_N)^2 + m_{\chi_1}m_N(\vec{v}_{\chi_1}-\vec{v}_{N_{out}})^2 = -(m_{\chi_2}-m_N)^2 + m_{\chi_2}m_N(\vec{v}_{\chi_2}-\vec{v}_{N_{in}})^2, \\
&-(m_{\chi_1}+m_N-m_{\chi_2})^2 - m_{\chi_1}m_N(\vec{v}_{\chi_1}-\vec{v}_{N_{in}})^2 + m_{\chi_1}m_{\chi_2}(\vec{v}_{\chi_1}-\vec{v}_{\chi_2})^2 \\
&\qquad\qquad + m_{\chi_2}m_N(\vec{v}_{\chi_2}-\vec{v}_{N_{in}})^2 = -m_N^2, \text{ and} \\
&-(m_{\chi_1}-m_{\chi_2})^2 + m_{\chi_1}m_{\chi_2}(\vec{v}_{\chi_1}-\vec{v}_{\chi_2})^2 = m_N^2(\vec{v}_{N_{in}}-\vec{v}_{N_{out}})^2.
\end{aligned}
\tag{A.3}
$$

From these relations we can substitute in the velocities from Eq. A.1 and solve for their dot products. These are, with the replacement $m_{\chi_2} \to m_{\chi_1}+\delta$,

$$
\begin{aligned}
\vec{v}_N \cdot \vec{v}_\chi &= v_\chi^2, \\
\vec{v}_N \cdot \vec{v}_{\rm el}^{\perp} &= -\frac{\delta\left((\delta+2m_{\chi_1})^2 + m_N^2 v_\chi^2\right)}{m_N(\delta+2m_{\chi_1})^2}, \text{ and} \\
\vec{v}_\chi \cdot \vec{v}_{\rm el}^{\perp} &= -\frac{\delta\left((\delta+2m_{\chi_1})^2\left(v_N^2 + 4(v_{\rm el}^{\perp})^2 + 8\right) + 4m_N^2 v_\chi^2\right)}{8m_N(\delta+2m_{\chi_1})^2}.
\end{aligned}
\tag{A.4}
$$

Also, because of the degrees of freedom and our choice of velocities there is a relation between v_N^2 and v_χ^2. This is obtained from the last momentum-conservation equation of Eq. A.2 and is

$$\frac{4m_{\chi_1}(m_{\chi_1}+\delta)m_N^2}{(2m_{\chi_1}+\delta)^2}v_\chi^2 = \delta^2 + m_N^2 v_N^2. \tag{A.5}$$

The final, orthogonal velocities are given by

$$\begin{aligned}
\vec{v}_N^{\perp} &= \vec{v}_N, \\
\vec{v}_\chi^{\perp} &= \vec{v}_\chi - \frac{\vec{v}_\chi \cdot \vec{v}_N^{\perp}}{(\vec{v}_N^{\perp})^2}\vec{v}_N^{\perp}, \text{ and} \\
\vec{v}_{\text{inel}}^{\perp} &= \vec{v}_{\text{el}}^{\perp} - \frac{\vec{v}_{\text{el}}^{\perp} \cdot \vec{v}_N^{\perp}}{|\vec{v}_N^{\perp}|^2}\vec{v}_N^{\perp} - \frac{\vec{v}_{\text{el}}^{\perp} \cdot \vec{v}_\chi^{\perp}}{|\vec{v}_\chi^{\perp}|^2}\vec{v}_\chi^{\perp}.
\end{aligned} \tag{A.6}$$

As stated in section 2.1, we are treating all momenta as order v and δ as order v^2, so the final forms for the velocity operators are, with $\vec{v}_N \to \vec{q}/m_N$,

$$\vec{v}_N^{\perp} = \frac{\vec{q}}{m_N}, \vec{v}_\chi^{\perp} = 0, \text{ and } \vec{v}_{\text{inel}}^{\perp} = \vec{v}_{\text{el}}^{\perp} + \frac{\delta}{|\vec{q}|^2}\vec{q}, \tag{A.7}$$

so we only have two velocity-like operators. As a check, these variables agree with section 2.1.

APPENDIX B

REDUCTION OF RELATIVISTIC OPERATORS

In this paper we have written the nonrelativistic reduction of many relativistic operators, but there are other possibilities not considered here (mainly interactions with spin 2 and beyond mediators). To help with the reduction of these other operators, we have included a series of reductions for the prototypical elements of a relativistic field theory. See [95] for similar results.

We concern ourselves with the spinor contractions

$$\bar{\psi}_2\psi_1, \quad \bar{\psi}_2\gamma^5\psi_1, \quad \bar{\psi}_2\gamma_\mu\gamma^5\psi_1,$$
$$\bar{\psi}_2\sigma_{\mu\nu}\psi_1, \text{ and } \quad \bar{\psi}_2\sigma_{\mu\nu}\gamma^5\psi_1,$$

where $\sigma_{\mu\nu} \equiv \frac{i}{2}[\gamma_\mu, \gamma_\nu]$.

In the nonrelativistic limit these become

$$\bar{\psi}_2\psi_1 \simeq 2\sqrt{m_1}\sqrt{m_2}\mathbf{1}_\psi, \tag{B.1}$$

$$\bar{\psi}_2\gamma^5\psi_1 \simeq 2\sqrt{m_1}\sqrt{m_2}(\vec{v}_1 - \vec{v}_2)\cdot\vec{S}_\psi, \tag{B.2}$$

$$\bar{\psi}_2\gamma_\mu\gamma^5\psi_1 \simeq 2\sqrt{m_1}\sqrt{m_2}(2S^i_\psi\delta^i_\mu - (\vec{v}_1 + \vec{v}_2)\cdot\vec{S}_\psi\delta^0_\mu), \tag{B.3}$$

$$\begin{aligned}\bar{\psi}_2\sigma_{\mu\nu}\psi_1 \simeq{}& \sqrt{m_1}\sqrt{m_2}4\epsilon_{ijk}S^k_\psi\delta^i_\mu\delta^j_\nu \\ &+ \sqrt{m_1}\sqrt{m_2}1(\delta^0_\mu\delta^a_\nu - \delta^a_\mu\delta^0_\nu)\left[-2i\epsilon_{aik}(\vec{v}_1 + \vec{v}_2)^i S^k_\psi + (\vec{v}_1 - \vec{v}_2)^a\right], \text{ and}\end{aligned} \tag{B.4}$$

$$\bar{\psi}_2\sigma_{\mu\nu}\gamma^5\psi_1 \simeq -\sqrt{m_1}\sqrt{m_2}4iS^i_\psi(\delta^0_\mu\delta^i_\nu - \delta^i_\mu\delta^0_\nu) \\ - \sqrt{m_1}\sqrt{m_2}\epsilon_{abc}\delta^a_\mu\delta^b_\nu\left[-2i\epsilon_{cid}(\vec{v}_1+\vec{v}_2)^i S^d_\psi + (\vec{v}_1-\vec{v}_2)^c\right]. \tag{B.5}$$

In these equations $\mathbf{1}_\psi$ is the unit operator in spin-space, $\vec{v}_1$ is the velocity of the incoming ψ_1 particle, $\vec{v}_2$ is the velocity of the outgoing ψ_2 particle, $\vec{S}_\psi$ is the spin operator for the ψ particle, $g_{\mu\nu}$ is the metric tensor, and ϵ_{ijk} is the Levi-Civita symbol. These reductions rely on ψ_1 in the initial state and ψ_2 in the final state (not their antiparticles) and that the only difference in these particles is the mass (m_1 and m_2 for initial and final respectively). One can also use the Gordon identity,

$$\bar{\psi}_1\gamma_\mu\psi_2 = \frac{1}{2\sqrt{m_1}\sqrt{m_2}}\bar{\psi}_1(p_{1\mu}+p_{2\mu}+i\sigma_{\mu\nu}q^\nu)\psi_2, \tag{B.6}$$

for the vector interaction.

Another useful result is the nonrelativistic limit for the time-like component of the momentum transfer, which is

$$q^0 \simeq \delta + \frac{m_{\chi_1}}{2}(\vec{v}^2_{\chi_2} - \vec{v}^2_{\chi_1}), \text{ or} \\ q^0 \simeq \frac{m_N}{2}(\vec{v}^2_{N_{in}} - \vec{v}^2_{N_{out}}). \tag{B.7}$$

These relations are sometimes needed for the preservation of Galilean invariance but can be easy to overlook.

To reduce operators for spin 1 particles we must take into account the polarization of a nonrelativistic vector boson. This is given by

$$\begin{aligned} \varepsilon^0_\lambda(\vec{p}) &\simeq \frac{\vec{p}}{m} \cdot \vec{\varepsilon}_\lambda(\vec{0}) \\ \vec{\varepsilon}_\lambda(\vec{p}) &\simeq \vec{\varepsilon}_\lambda(\vec{0}), \end{aligned} \tag{B.8}$$

to lowest order in $\vec{p}$.

APPENDIX C

TRANSITION AMPLITUDE IN NUCLEAR RESPONSE BASIS

Since the effective theory for inelastic dark matter is so similar to the effective theory for elastic dark matter, it can be easy to overlook some of the important differences. The change in the Galilean-invariant incoming dark matter velocity is stressed above, but the possible complex nature for the coefficients of the nonrelativistic operators Eq. 2.8 is another modification. To highlight both of these effects we reproduce the relevant results for the squared matrix element, following [32].

First we write our Lagrangian as

$$\mathcal{L} = \sum_{\tau=0,1} \sum_{i=1}^{15} c_i^\tau \mathcal{O}_i, \tag{C.1}$$

where τ characterizes the isospin structure of the coupling, allowing different couplings to protons and neutrons. We then calculate the transition amplitude, by averaging over initial spins and summing over outgoing spins, and expand in the basis of the

nuclear responses, giving

$$\begin{aligned}
\frac{1}{2j_\chi+1}\frac{1}{2j_N+1}\sum_{\text{spins}}|\mathcal{M}|^2_{\text{nuclear}} &= \frac{4\pi}{2j_N+1}\sum_{\tau=0,1}\sum_{\tau'=0,1}\Bigg\{ \\
&\sum_{J=0,2,\ldots}^{\infty}\Bigg[R_M^{\tau\tau'}(|\vec{v}^{\perp}_{\text{inel}\,T}|^2,\frac{|\vec{q}|^2}{m_N^2})\langle j_N||M_{J;\tau}(q)||j_N\rangle\langle j_N||M_{J;\tau'}(q)||j_N\rangle \\
&\quad+\frac{|\vec{q}|^2}{m_N^2}R_{\Phi''}^{\tau\tau'}(|\vec{v}^{\perp}_{\text{inel}\,T}|^2,\frac{|\vec{q}|^2}{m_N^2})\langle j_N||\Phi''_{J;\tau}(q)||j_N\rangle\langle j_N||\Phi''_{J;\tau'}(q)||j_N\rangle \\
&\quad+\frac{|\vec{q}|^2}{m_N^2}R_{\Phi''M}^{\tau\tau'}(|\vec{v}^{\perp}_{\text{inel}\,T}|^2,\frac{|\vec{q}|^2}{m_N^2})\langle j_N||\Phi''_{J;\tau}(q)||j_N\rangle\langle j_N||M_{J;\tau'}(q)||j_N\rangle\Bigg] \\
&+\sum_{J=2,4,\ldots}^{\infty}\left[\frac{|\vec{q}|^2}{m_N^2}R_{\tilde{\Phi}'}^{\tau\tau'}(|\vec{v}^{\perp}_{\text{inel}\,T}|^2,\frac{|\vec{q}|^2}{m_N^2})\langle j_N||\tilde{\Phi}'_{J;\tau}(q)||j_N\rangle\langle j_N||\tilde{\Phi}'_{J;\tau'}(q)||j_N\rangle\right] \\
&+\sum_{J=1,3,\ldots}^{\infty}\Bigg[R_{\Sigma''}^{\tau\tau'}(|\vec{v}^{\perp}_{\text{inel}\,T}|^2,\frac{|\vec{q}|^2}{m_N^2})\langle j_N||\Sigma''_{J;\tau}(q)||j_N\rangle\langle j_N||\Sigma''_{J;\tau'}(q)||j_N\rangle \\
&\quad+R_{\Sigma'}^{\tau\tau'}(|\vec{v}^{\perp}_{\text{inel}\,T}|^2,\frac{|\vec{q}|^2}{m_N^2})\langle j_N||\Sigma'_{J;\tau}(q)||j_N\rangle\langle j_N||\Sigma'_{J;\tau'}(q)||j_N\rangle \\
&\quad+\frac{|\vec{q}|^2}{m_N^2}R_{\Delta}^{\tau\tau'}(|\vec{v}^{\perp}_{\text{inel}\,T}|^2,\frac{|\vec{q}|^2}{m_N^2})\langle j_N||\Delta_{J;\tau}(q)||j_N\rangle\langle j_N||\Delta_{J;\tau'}(q)||j_N\rangle \\
&\quad+\frac{|\vec{q}|^2}{m_N^2}R_{\Delta\Sigma'}^{\tau\tau'}(|\vec{v}^{\perp}_{\text{inel}\,T}|^2,\frac{|\vec{q}|^2}{m_N^2})\langle j_N||\Delta_{J;\tau}(q)||j_N\rangle\langle j_N||\Sigma'_{J;\tau'}(q)||j_N\rangle\Bigg]\Bigg\}.
\end{aligned} \tag{C.2}$$

This result is expanded in spherical harmonics leading to the nuclear operators $M, \Delta, \Sigma', \Sigma'', \tilde{\Phi}', \Phi''$. The inelastic kinematics does not modify these operators, so we do not reproduce their expressions. Instead, the changes are solely in the R

coefficients

$$
\begin{aligned}
R_M^{\tau\tau'}(|\vec{v}_T|^2, \frac{|\vec{q}|^2}{m_N^2}, \delta) &= c_1^\tau c_1^{\tau'*} + \frac{j_\chi(j_\chi+1)}{3}\Bigg[\left(\frac{|\vec{q}|^2}{m_N^2}c_5^\tau c_5^{\tau'*} + c_8^\tau c_8^{\tau'*}\right) \\
&\quad \times \left(|\vec{v}_T|^2 - v_{\min T}^2(\delta)\right) + \frac{|\vec{q}|^2}{m_N^2}c_{11}^\tau c_{11}^{\tau'*}\Bigg] \\
R_{\Phi''}^{\tau\tau'}(|\vec{v}_T|^2, \frac{|\vec{q}|^2}{m_N^2}, \delta) &= \frac{1}{4}\frac{|\vec{q}|^2}{m_N^2}c_3^\tau c_3^{\tau'*} + \frac{j_\chi(j_\chi+1)}{12}\left(c_{12}^\tau - \frac{|\vec{q}|^2}{m_N^2}c_{15}^\tau\right)\left(c_{12}^{\tau'*} - \frac{|\vec{q}|^2}{m_N^2}c_{15}^{\tau'*}\right) \\
R_{\Phi''M}^{\tau\tau'}(|\vec{v}_T|^2, \frac{|\vec{q}|^2}{m_N^2}, \delta) &= \mathrm{Re}\left[c_3^\tau c_1^{\tau'*} + \frac{j_\chi(j_\chi+1)}{3}\left(c_{12}^\tau - \frac{|\vec{q}|^2}{m_N^2}c_{15}^\tau\right)c_{11}^{\tau'*}\right] \\
R_{\tilde{\Phi}'}^{\tau\tau'}(|\vec{v}_T|^2, \frac{|\vec{q}|^2}{m_N^2}, \delta) &= \frac{j_\chi(j_\chi+1)}{12}\left[c_{12}^\tau c_{12}^{\tau'*} + \frac{|\vec{q}|^2}{m_N^2}c_{13}^\tau c_{13}^{\tau'*}\right] \\
R_{\Sigma''}^{\tau\tau'}(|\vec{v}_T|^2, \frac{|\vec{q}|^2}{m_N^2}, \delta) &= \frac{1}{4}\frac{|\vec{q}|^2}{m_N^2}c_{10}^\tau c_{10}^{\tau'*} + \frac{j_\chi(j_\chi+1)}{12}\Bigg[c_4^\tau c_4^{\tau'*} + \frac{|\vec{q}|^2}{m_N^2}\left(c_4^\tau c_6^{\tau'*} + c_6^\tau c_4^{\tau'*}\right) \\
&\quad + \frac{|\vec{q}|^4}{m_N^4}c_6^\tau c_6^{\tau'*} + \left(c_{12}^\tau c_{12}^{\tau'*} + \frac{|\vec{q}|^2}{m_N^2}c_{13}^\tau c_{13}^{\tau'*}\right)\left(|\vec{v}_T|^2 - v_{\min T}^2(\delta)\right)\Bigg] \\
R_{\Sigma'}^{\tau\tau'}(|\vec{v}_T|^2, \frac{|\vec{q}|^2}{m_N^2}, \delta) &= \frac{1}{8}\left[\frac{|\vec{q}|^2}{m_N^2}c_3^\tau c_3^{\tau'*} + c_7^\tau c_7^{\tau'*}\right]\left(|\vec{v}_T|^2 - v_{\min T}^2(\delta)\right) + \frac{j_\chi(j_\chi+1)}{12} \\
&\quad \times \Bigg\{c_4^\tau c_4^{\tau'*} \quad + \frac{|\vec{q}|^2}{m_N^2}c_9^\tau c_9^{\tau'*} + \frac{1}{2}\Bigg[\left(c_{12}^\tau - \frac{|\vec{q}|^2}{m_N^2}c_{15}^\tau\right)\left(c_{12}^{\tau'*} - \frac{|\vec{q}|^2}{m_N^2}c_{15}^{\tau'*}\right) \\
&\quad + \frac{|\vec{q}|^2}{m_N^2}c_{14}^\tau c_{14}^{\tau'*}\Bigg]\left(|\vec{v}_T|^2 - v_{\min T}^2(\delta)\right)\Bigg\} \\
R_{\Delta}^{\tau\tau'}(|\vec{v}_T|^2, \frac{|\vec{q}|^2}{m_N^2}, \delta) &= \frac{j_\chi(j_\chi+1)}{3}\left[\frac{|\vec{q}|^2}{m_N^2}c_5^\tau c_5^{\tau'*} + c_8^\tau c_8^{\tau'*}\right] \\
R_{\Delta\Sigma'}^{\tau\tau'}(|\vec{v}_T|^2, \frac{|\vec{q}|^2}{m_N^2}, \delta) &= \frac{j_\chi(j_\chi+1)}{3}\mathrm{Re}\left[c_5^\tau c_4^{\tau'*} - c_8^\tau c_9^{\tau'*}\right].
\end{aligned}
\tag{C.3}
$$

Here we have expanded $|\vec{v}_{\mathrm{inel}\,T}^{\perp}|^2$ as in Eq. 2.13 to show the dependence on δ, and we have also included the appropriate complex conjugation of the coefficients as relativistic inelastic dark matter operators can produce complex coefficients for their nonrelativistic counterparts.

REFERENCES CITED

[1] Georges Aad et al. Observation of a new particle in the search for the Standard Model Higgs boson with the ATLAS detector at the LHC. *Phys. Lett.*, B716:1–29, 2012.

[2] K. Abe et al. Precise Measurement of the Neutrino Mixing Parameter θ_{23} from Muon Neutrino Disappearance in an Off-Axis Beam. *Phys. Rev. Lett.*, 112(18):181801, 2014.

[3] Doe science drivers of particle physics. `http://science.energy.gov/hep/research/science-drivers-of-particle-physics/`. Accessed: 2016-4-18.

[4] Katherine Garrett and Gintaras Duda. Dark Matter: A Primer. *Adv. Astron.*, 2011:968283, 2011.

[5] Marusa Bradac, Douglas Clowe, Anthony H. Gonzalez, Phil Marshall, William Forman, Christine Jones, Maxim Markevitch, Scott Randall, Tim Schrabback, and Dennis Zaritsky. Strong and weak lensing united. 3. Measuring the mass distribution of the merging galaxy cluster 1E0657-56. *Astrophys. J.*, 652:937–947, 2006.

[6] Bharat Ratra, Radoslaw Stompor, Ken Ganga, Graca Rocha, Naoshi Sugiyama, and Krzysztof M. Gorski. CMB anisotropy constraints on open and flat lambda CDM cosmogonies from UCSB south pole, ARGO, MAX, white dish, and SuZIE data. *Astrophys. J.*, 517:549, 1999.

[7] R. Bernabei, P. Belli, F. Cappella, V. Caracciolo, S. Castellano, et al. Final model independent result of DAMA/LIBRA-phase1. *Eur.Phys.J.*, C73:2648, 2013.

[8] Lisa Goodenough and Dan Hooper. Possible Evidence For Dark Matter Annihilation In The Inner Milky Way From The Fermi Gamma Ray Space Telescope. 2009.

[9] M. Ajello et al. Fermi-LAT Observations of High-Energy γ-Ray Emission Toward the Galactic Center. *Astrophys. J.*, 819(1):44, 2016.

[10] M. Aguilar et al. First Result from the Alpha Magnetic Spectrometer on the International Space Station: Precision Measurement of the Positron Fraction in Primary Cosmic Rays of 0.5?350 GeV. *Phys. Rev. Lett.*, 110:141102, 2013.

[11] A. Liam Fitzpatrick, Wick Haxton, Emanuel Katz, Nicholas Lubbers, and Yiming Xu. The Effective Field Theory of Dark Matter Direct Detection. *JCAP*, 1302:004, 2013.

[12] Clifford Cheung, Paolo Creminelli, A. Liam Fitzpatrick, Jared Kaplan, and Leonardo Senatore. The Effective Field Theory of Inflation. *JHEP*, 03:014, 2008.

[13] David Tucker-Smith and Neal Weiner. Inelastic dark matter. *Phys.Rev.*, D64:043502, 2001.

[14] Bob Holdom. Two U(1)'s and Epsilon Charge Shifts. *Phys.Lett.*, B166:196, 1986.

[15] Nima Arkani-Hamed, Douglas P. Finkbeiner, Tracy R. Slatyer, and Neal Weiner. A Theory of Dark Matter. *Phys.Rev.*, D79:015014, 2009.

[16] Maxim Pospelov. Secluded u(1) below the weak scale. *Phys. Rev. D*, 80:095002, Nov 2009.

[17] Oscar Adriani et al. An anomalous positron abundance in cosmic rays with energies 1.5-100 GeV. *Nature*, 458:607–609, 2009.

[18] M. Ackermann et al. Measurement of separate cosmic-ray electron and positron spectra with the Fermi Large Area Telescope. *Phys. Rev. Lett.*, 108:011103, 2012.

[19] H. Merkel et al. Searches for dark photons at the Mainz Microtron. *AIP Conf. Proc.*, 1563:143–146, 2013.

[20] G. Barello, Spencer Chang, and Christopher A. Newby. A Model Independent Approach to Inelastic Dark Matter Scattering. *Phys. Rev.*, D90(9):094027, 2014.

[21] G. Barello, Spencer Chang, and Christopher A. Newby. Correlated Signals at the Energy and Intensity Frontiers from Nonabelian Kinetic Mixing. 2015.

[22] Mark W. Goodman and Edward Witten. Detectability of Certain Dark Matter Candidates. *Phys.Rev.*, D31:3059, 1985.

[23] P. Cushman, C. Galbiati, D.N. McKinsey, H. Robertson, T.M.P. Tait, et al. Working Group Report: WIMP Dark Matter Direct Detection. 2013.

[24] Spencer Chang, Aaron Pierce, and Neal Weiner. Momentum Dependent Dark Matter Scattering. *JCAP*, 1001:006, 2010.

[25] Brian Feldstein, A. Liam Fitzpatrick, and Emanuel Katz. Form Factor Dark Matter. *JCAP*, 1001:020, 2010.

[26] Yang Bai and Patrick J. Fox. Resonant Dark Matter. *JHEP*, 0911:052, 2009.

[27] Maxim Khlopov. Dark atoms and puzzles of dark matter searches. *Int.J.Mod.Phys.*, A29:1443002, 2014.

[28] Spencer Chang, Jia Liu, Aaron Pierce, Neal Weiner, and Itay Yavin. CoGeNT Interpretations. *JCAP*, 1008:018, 2010.

[29] Jonathan L. Feng, Jason Kumar, Danny Marfatia, and David Sanford. Isospin-Violating Dark Matter. *Phys.Lett.*, B703:124–127, 2011.

[30] Vincenzo Cirigliano, Michael L. Graesser, Grigory Ovanesyan, and Ian M. Shoemaker. Shining LUX on Isospin-Violating Dark Matter Beyond Leading Order. 2013.

[31] JiJi Fan, Matthew Reece, and Lian-Tao Wang. Non-relativistic effective theory of dark matter direct detection. *JCAP*, 1011:042, 2010.

[32] Nikhil Anand, A. Liam Fitzpatrick, and W.C. Haxton. Model-independent WIMP Scattering Responses and Event Rates: A Mathematica Package for Experimental Analysis. 2013.

[33] A. Liam Fitzpatrick, Wick Haxton, Emanuel Katz, Nicholas Lubbers, and Yiming Xu. Model Independent Direct Detection Analyses. 2012.

[34] Marco Cirelli, Eugenio Del Nobile, and Paolo Panci. Tools for model-independent bounds in direct dark matter searches. *JCAP*, 1310:019, 2013.

[35] Moira I. Gresham and Kathryn M. Zurek. On the Effect of Nuclear Response Functions in Dark Matter Direct Detection. *Phys.Rev.*, D89:123521, 2014.

[36] Riccardo Catena and Paolo Gondolo. Global fits of the dark matter-nucleon effective interactions. 2014.

[37] Vera Gluscevic and Annika H. G. Peter. Understanding WIMP-baryon interactions with direct detection: A Roadmap. 2014.

[38] Chiara Arina, Eugenio Del Nobile, and Paolo Panci. Not so Coy Dark Matter explains DAMA (and the Galactic Center excess). 2014.

[39] David Tucker-Smith and Neal Weiner. The Status of inelastic dark matter. *Phys.Rev.*, D72:063509, 2005.

[40] Douglas P. Finkbeiner, Tracy R. Slatyer, Neal Weiner, and Itay Yavin. PAMELA, DAMA, INTEGRAL and Signatures of Metastable Excited WIMPs. *JCAP*, 0909:037, 2009.

[41] Rouven Essig, Jared Kaplan, Philip Schuster, and Natalia Toro. On the Origin of Light Dark Matter Species. *Submitted to Physical Review D*, 2010.

[42] Peter W. Graham, Roni Harnik, Surjeet Rajendran, and Prashant Saraswat. Exothermic Dark Matter. *Phys.Rev.*, D82:063512, 2010.

[43] Spencer Chang, Neal Weiner, and Itay Yavin. Magnetic Inelastic Dark Matter. *Phys.Rev.*, D82:125011, 2010.

[44] Tao Han and Ralf Hempfling. Messenger sneutrinos as cold dark matter. *Phys.Lett.*, B415:161–169, 1997.

[45] Lawrence J. Hall, Takeo Moroi, and Hitoshi Murayama. Sneutrino cold dark matter with lepton number violation. *Phys.Lett.*, B424:305–312, 1998.

[46] Yanou Cui, David E. Morrissey, David Poland, and Lisa Randall. Candidates for Inelastic Dark Matter. *JHEP*, 0905:076, 2009.

[47] Daniele S.M. Alves, Siavosh R. Behbahani, Philip Schuster, and Jay G. Wacker. Composite Inelastic Dark Matter. *Phys.Lett.*, B692:323–326, 2010.

[48] David E. Kaplan, Gordan Z. Krnjaic, Keith R. Rehermann, and Christopher M. Wells. Atomic Dark Matter. *JCAP*, 1005:021, 2010.

[49] Kunal Kumar, Arjun Menon, and Tim M.P. Tait. Magnetic Fluffy Dark Matter. *JHEP*, 1202:131, 2012.

[50] Haipeng An, P.S. Bhupal Dev, Yi Cai, and R.N. Mohapatra. Sneutrino Dark Matter in Gauged Inverse Seesaw Models for Neutrinos. *Phys.Rev.Lett.*, 108:081806, 2012.

[51] J. Angle et al. Constraints on inelastic dark matter from XENON10. *Phys.Rev.*, D80:115005, 2009.

[52] E. Aprile et al. Dark Matter Results from 225 Live Days of XENON100 Data. *Phys.Rev.Lett.*, 109:181301, 2012.

[53] D.S. Akerib et al. First results from the LUX dark matter experiment at the Sanford Underground Research Facility. *Phys.Rev.Lett.*, 112:091303, 2014.

[54] Z. Ahmed et al. Search for inelastic dark matter with the CDMS II experiment. *Phys.Rev.*, D83:112002, 2011.

[55] E. Behnke et al. First Dark Matter Search Results from a 4-kg CF_3I Bubble Chamber Operated in a Deep Underground Site. *Phys.Rev.*, D86:052001, 2012.

[56] S.C. Kim, H. Bhang, J.H. Choi, W.G. Kang, B.H. Kim, et al. New Limits on Interactions between Weakly Interacting Massive Particles and Nucleons Obtained with CsI(Tl) Crystal Detectors. *Phys.Rev.Lett.*, 108:181301, 2012.

[57] G. Angloher, M. Bauer, I. Bavykina, A. Bento, C. Bucci, et al. Results from 730 kg days of the CRESST-II Dark Matter Search. *Eur.Phys.J.*, C72:1971, 2012.

[58] Jo Bovy and Scott Tremaine. On the local dark matter density. *Astrophys.J.*, 756:89, 2012.

[59] F. J. Kerr and D. Lynden-Bell. Review of galactic constants. *Mon.Not.Roy.Astron.Soc.*, 221:1023–1038, August 1986.

[60] Martin C. Smith, G.R. Ruchti, A. Helmi, R.F.G. Wyse, J.P. Fulbright, et al. The RAVE Survey: Constraining the Local Galactic Escape Speed. *Mon.Not.Roy.Astron.Soc.*, 379:755–772, 2007.

[61] R. Bernabei, P. Belli, V. Landoni, F. Montecchia, W. Di Nicolantonio, et al. New limits on WIMP search with large-mass low-radioactivity NaI(Tl) set-up at Gran Sasso. *Phys.Lett.*, B389:757–766, 1996.

[62] J.I. Collar. Quenching and channeling of nuclear recoils in NaI(Tl): Implications for dark-matter searches. *Phys.Rev.*, C88(3):035806, 2013.

[63] E. Behnke et al. Direct Measurement of the Bubble Nucleation Energy Threshold in a CF3I Bubble Chamber. *Phys.Rev.*, D88:021101, 2013.

[64] H. Park, D.H. Choi, J.M. Choi, I.S. Hahn, M.J. Hwang, et al. Neutron beam test of CsI crystal for dark matter search. *Nucl.Instrum.Meth.*, A491:460–469, 2002.

[65] J.I. Collar, N.E. Fields, E. Fuller, M. Hai, T.W. Hossbach, et al. Coherent neutrino-nucleus scattering detection with a CsI[Na] scintillator at the SNS spallation source. 2014.

[66] Joachim Kopp, Thomas Schwetz, and Jure Zupan. Global interpretation of direct Dark Matter searches after CDMS-II results. *JCAP*, 1002:014, 2010.

[67] Karin Dissauer, Mads T. Frandsen, Tuomas Hapola, and Francesco Sannino. Perturbative extension of the standard model with a 125 GeV Higgs boson and magnetic dark matter. *Phys.Rev.*, D87(3):035005, 2013.

[68] Neal Weiner and Itay Yavin. UV Completions of Magnetic Inelastic Dark Matter and RayDM for the Fermi Line(s). *Phys.Rev.*, D87:023523, 2013.

[69] Peter Galison and Aneesh Manohar. TWO Z's OR NOT TWO Z's? *Phys. Lett.*, B136:279, 1984.

[70] Nima Arkani-Hamed and Neal Weiner. LHC Signals for a SuperUnified Theory of Dark Matter. *JHEP*, 12:104, 2008.

[71] Maxim Pospelov, Adam Ritz, and Mikhail B. Voloshin. Secluded WIMP Dark Matter. *Phys. Lett.*, B662:53–61, 2008.

[72] Rouven Essig et al. Working Group Report: New Light Weakly Coupled Particles. In *CSS 2013: Snowmass*, 2013.

[73] Witold Skiba. Effective Field Theory and Precision Electroweak Measurements. pages 5–70, 2011.

[74] Rouven Essig, Philip Schuster, Natalia Toro, and Bogdan Wojtsekhowski. An Electron Fixed Target Experiment to Search for a New Vector Boson A' Decaying to e+e-. *JHEP*, 02:009, 2011.

[75] Andrea Celentano. The Heavy Photon Search experiment at Jefferson Laboratory. *J. Phys. Conf. Ser.*, 556(1):012064, 2014.

[76] J.P. Lees et al. Search for a Dark Photon in e^+e^- Collisions at BaBar. *Phys.Rev.Lett.*, 113(20):201801, 2014.

[77] Vindhyawasini Prasad, Haibo Li, and Xinchou Lou. Search for low-mass Higgs and dark photons at BESIII. 2015.

[78] Philip Ilten, Jesse Thaler, Mike Williams, and Wei Xue. Dark photons from charm mesons at LHCb. 2015.

[79] L. Lavoura and Ling-Fong Li. Making the small oblique parameters large. *Phys. Rev.*, D49:1409–1416, 1994.

[80] K.A. Olive et al. Review of Particle Physics. *Chin.Phys.*, C38:090001, 2014.

[81] Adam Alloul, Neil D. Christensen, Cline Degrande, Claude Duhr, and Benjamin Fuks. FeynRules 2.0 - A complete toolbox for tree-level phenomenology. *Comput. Phys. Commun.*, 185:2250–2300, 2014.

[82] Alexander Belyaev, Neil D. Christensen, and Alexander Pukhov. CalcHEP 3.4 for collider physics within and beyond the Standard Model. *Comput. Phys. Commun.*, 184:1729–1769, 2013.

[83] Georges Aad et al. A search for prompt lepton-jets in pp collisions at $\sqrt{s} = 7$ TeV with the ATLAS detector. *Phys. Lett.*, B719:299–317, 2013.

[84] Vardan Khachatryan et al. A Search for Pair Production of New Light Bosons Decaying into Muons. 2015.

[85] Georges Aad et al. A search for prompt lepton-jets in pp collisions at $\sqrt{s} = 8$ TeV with the ATLAS detector. 2015.

[86] Measurements of the Higgs boson production and decay rates and constraints on its couplings from a combined ATLAS and CMS analysis of the LHC pp collision data at sqrt(s) = 7 and 8 TeV. Technical Report ATLAS-CONF-2015-044, CERN, Geneva, Sep 2015.

[87] David Curtin, Rouven Essig, Stefania Gori, and Jessie Shelton. Illuminating Dark Photons with High-Energy Colliders. *JHEP*, 02:157, 2015.

[88] Georges Aad et al. Search for new light gauge bosons in Higgs boson decays to four-lepton final states in pp collisions at $\sqrt{s} = 8$ TeV with the ATLAS detector at the LHC. 2015.

[89] Georges Aad et al. Evidence for Electroweak Production of $W^{\pm}W^{\pm}jj$ in pp Collisions at $\sqrt{s} = 8$ TeV with the ATLAS Detector. *Phys. Rev. Lett.*, 113(14):141803, 2014.

[90] Georges Aad et al. Search for long-lived neutral particles decaying into lepton jets in proton-proton collisions at $\sqrt{s} = 8$ TeV with the ATLAS detector. *JHEP*, 11:088, 2014.

[91] J. Alwall, R. Frederix, S. Frixione, V. Hirschi, F. Maltoni, O. Mattelaer, H. S. Shao, T. Stelzer, P. Torrielli, and M. Zaro. The automated computation of tree-level and next-to-leading order differential cross sections, and their matching to parton shower simulations. *JHEP*, 07:079, 2014.

[92] Torbjrn Sjstrand, Stefan Ask, Jesper R. Christiansen, Richard Corke, Nishita Desai, Philip Ilten, Stephen Mrenna, Stefan Prestel, Christine O. Rasmussen, and Peter Z. Skands. An Introduction to PYTHIA 8.2. *Comput. Phys. Commun.*, 191:159–177, 2015.

[93] J. de Favereau, C. Delaere, P. Demin, A. Giammanco, V. Lematre, A. Mertens, and M. Selvaggi. DELPHES 3, A modular framework for fast simulation of a generic collider experiment. *JHEP*, 02:057, 2014.

[94] David Curtin, Jamison Galloway, and Jay G. Wacker. Measuring the $t\bar{t}h$ coupling from same-sign dilepton $+2b$ measurements. *Phys. Rev.*, D88(9):093006, 2013.

[95] Jason Kumar and Danny Marfatia. Matrix element analyses of dark matter scattering and annihilation. *Phys.Rev.*, D88(1):014035, 2013.